

Deposition Modeling for Paint Application on Surfaces Embedded in \mathbb{R}^3

David C. Conner Prasad N. Atkar Alfred A. Rizzi Howie Choset

CMU-RI-TR-02-08

October 2002

Robotics Institute
Carnegie Mellon University
Pittsburgh, Pennsylvania 15213

© Carnegie Mellon University

Abstract

As part of an ongoing collaborative effort with the Ford Motor Company, our research aims to develop practical and efficient trajectory planning tools for automotive painting. Not only must the paint applicator pass over all points on the surface, it must do so in a manner that ensures the uniformity of the coating thickness. This is non-trivial given the complexity of automotive surfaces. This report documents our efforts to develop analytic deposition models for electrostatic rotating bell (ESRB) atomizers, which have recently become widely used in the automotive painting industry. Conventional deposition models, used in earlier automatic trajectory planning tools, fail to capture the complexity of deposition patterns generated by ESRB atomizers. The models presented here take into account both the surface curvature and the deposition pattern of ESRB atomizers, enabling planning tools to optimize atomizer trajectories to meet several measures of quality, such as coating uniformity. In addition to the development of our models, we present experimental results used to evaluate our models, and verify the interaction between the deposition pattern, trajectory, and surface curvature.

Contents

1	Introduction	1
2	Prior Work	1
2.1	Trajectory Planning	2
2.2	Deposition Simulation	4
3	Deposition Modeling	5
3.1	2D Deposition Model	6
3.1.1	Planar Deposition Model	7
3.1.2	Surface Projection Model	8
3.2	1D Collapse Model	11
3.2.1	Planar Thickness Variation Calculation	12
3.2.2	Cylindrical Thickness Variation Calculation	17
4	Experimental Validation	24
4.1	Deposition Model Parameterization	24
4.2	Planar Deposition Results	24
4.3	Surface Deposition Results	25
4.4	Miscellaneous Results	26
5	Conclusions	29
6	Acknowledgments	29
References		31
A	Revised Asymmetry Term for 2D Deposition Model	33
B	Experimental Data	35

1 Introduction

The application of paint in the automotive industry is a critical step in the assembly process. The paint must be applied in a uniform manner, as excessive variation in coating thickness is visible to the human eye and leads to customer rejection [1]. The paint applicator trajectories must be planned in such a way as to guarantee complete coverage, while minimizing thickness variation. Additionally, the painting process is subject to severe economic and environmental penalties for inefficiency. Since strict environmental regulations limit the amount of exhaust from the painting process, any reduction in the total amount of paint sprayed directly impacts both the environment and the economics. This limits the amount of over spray and start/stops (triggering) of the paint applicator.

Industrial robots are widely used for automotive paint application because of the repeatability of the surface finish, along with the removal of humans from a hazardous environment. The task of applying automotive paint has moved further beyond human capabilities with the advent of high speed rotating bell atomizers and electrostatic charging, both used to increase transfer efficiency. While applying paint is purely robotic, generating trajectories for the robots is largely a human endeavor based on the experience of skilled technicians. The planning tools widely available, such as RobCAD™ Paint, are limited to simple paths on 2D silhouettes, which are then projected back onto the 3D automotive surface. Although the use of simulation software has cut the amount of validation required on vehicles, the process still requires significant trial and error. Since the final paths cannot be generated until the body design is finalized –which is one of the last items in the design process– the development of good painting plans represents a bottleneck in the concept-to-customer time-line. Any progress in automating this task ultimately decreases the total time required to bring a new concept to the customer.

In addition to time savings, the automatic generation of trajectories allows for the evaluation of trajectories against a set of specified criteria. Trajectories that are planned for the robots must yield paint deposition that is both complete in its coverage, and sufficiently uniform so that the variation in thickness is not noticeable and does not degrade the mechanical properties of the coating. By planning trajectories that limit the required amount of paint sprayed off the surface, and the amount of start/stop cycles of the paint flow, paths more efficient from the standpoint of total paint usage can be generated.

In this report we discuss our initial steps toward solving the problem of automatically generating trajectories for automotive painting on arbitrary surfaces. The complicated deposition patterns generated by rotating bell atomizers have made previous work in trajectory planning inadequate, therefore this report outlines the development of analytic models of deposition patterns for this class of paint applicators, and discusses the impact of the structure of these patterns on path planning. Section 2 covers relevant prior work for this research, including both deposition modeling and trajectory planning for paint application. In Section 3, we develop analytic models of the deposition pattern generated by high speed rotating bell atomizers, widely used for automotive painting. We further develop an analytic relation between the structure of the deposition pattern and the variability of the paint thickness. In Section 4, we discuss experimental tests and methods used to determine values for the parameters of the analytic models . Further results of experiments designed to validate the parameterized models developed in Section 3 are also presented. Finally, in Section 5 we draw conclusions from the results and discuss the future direction of our work.

2 Prior Work

The work that we present in this report is an outgrowth of our prior work in the area of coverage planning [2, 3]. Our earlier work developed plans for guaranteeing complete coverage of an unknown area, and was

later lifted to surfaces embedded in \mathbb{R}^3 [4]. While this prior work guaranteed complete coverage, it did not necessarily yield uniform coverage. Our work now focuses on the task of planning trajectories in a way that guarantees complete coverage, while at the same time minimizing coating thickness variation. The remainder of this section discusses prior work in two broad areas that overlap with our current focus: trajectory planning and deposition modeling.

2.1 Trajectory Planning

An early attempt at automated trajectory planning for painting robots was the Automatic Trajectory Planning System (ATPS) [5]. The system took CAD data in the form of B-splines or Bezier surfaces, and planned robot paths that followed in the direction of least curvature. The velocity profile along the path was determined to optimize coating uniformity and total painting time given the planned paths. The paint deposition pattern was assumed to be circular, with a uniform distribution within the circle. Paint distribution on the surface was based on the intersection of a surface point with the spray cone. This highly simplified deposition model limited the utility of the method in industrial application.

A “teachless” spray painting system was developed by Asakawa and Takeuchi [6]. A series of spray painting points were input into the CAD data, and the system automatically generated the required paths, including off the surface (over spray) points. The system required a set of parameters such as the elliptical diameters of the paint pattern and the desired distance between consecutive passes, which is known as the *index distance*. A deposition model was not given; apparently the required parameters were determined experimentally. No information was given about how the parameters were estimated, or how to adapt them to new surface shapes.

Researchers at the University of Dortmund proposed a generalized framework for off-line programming of robots [7]. In this work they use the example of painting robots, and propose a simple bivariate Gaussian model for the paint deposition. Their work considers the optimum index distance, and calculates the distance based on the Gaussian deposition pattern. The work does not consider surface effects or complicated deposition patterns.

Sheng *et al.* developed an automated CAD-guided planning system for spray painting [8]. Their work used a simplified paint deposition model, without an explicit dependence on the surface being painted. The path planning algorithm depended on a user-defined index distance, and was verified using RobCAD™ Paint software. In later work, Sheng *et al.* extended their prior work to consider the effects of surface curvature in a limited manner [9]. This work formed patches where the surface normals of triangular elements used to approximate the given surface were within certain bounds. The bound was based on a maximum deviation angle between the surface element normal and the paint gun normal. The patches and gun orientation were iteratively solved to give an acceptable paint deposition pattern. The work does not address stitching the approximately planar patches together, nor does it address generating trajectories over highly curved sections. The deposition model assumed a simple parabolic thickness profile with a circular deposition pattern.

Arikan and Balkan developed a paint deposition simulation where the paint deposition model used a beta distribution, shown in Figure 1 [10]. The paper considered the effect of the distribution pattern on the optimal index distance, along with a preliminary attempt at considering surface effects on the deposition. The developed spray pattern assumes an aerosol spray, and is not appropriate for rotating bell atomizers.

An automatic trajectory generation system for unknown parts has been developed which uses scanning laser range finders to detect parts and their salient features [11]. Features—such as planes, cylinders, and cavities—were detected from range data, and trajectories were stitched together based on plans for each feature type. This work was only concerned with coverage, and did not address deposition models or thickness variation.

Hertling *et al.* report on research at Odense University in Denmark to develop an automated “task curve planner” for painting robots in a shipyard environment [12]. Part of the motivation is the prohibitive cost of robot programming for small numbers of painting runs on custom parts. The cited paper focused on the development of the deposition models, which fit a series of basis functions to the experimental data assuming an elliptical pattern. Hertling *et al.* report that the observed deposition patterns were not uniform, and did not exhibit a parabolic profile as reported by other researchers. Although the final work is not published at this time, the researchers have demonstrated using their models in numeric optimization to plan paths on flat plates. For more information see <http://www.mip.sdu.dk/research/Smartpainter/index.html>. The work assumes aerosol sprays, with the authors specifically excluding electrostatic sprays because of the inherent complexity of the deposition pattern.

Ramabhadran and Antonio present a framework for efficient optimization of trajectories for painting applications [13]. Their work focuses on the organization of the optimization problem, assuming a general form for the deposition model. In their work, the deposition model is assumed to be either a bivariate Cauchy or Gaussian distribution (Figure 1) applied to a flat panel. This work focuses on the efficiency of the optimization technique, and does not cover new ground in developing realistic deposition models.

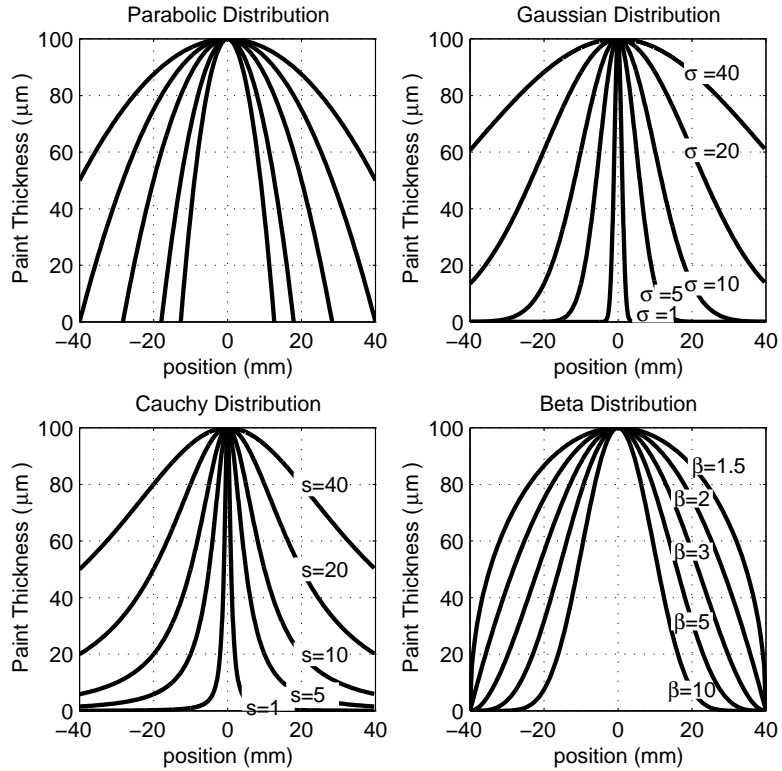


Figure 1: Simple deposition patterns typically used in previous research. Cauchy distributions are similar to Gaussian distributions, but have thinner peaks and fatter tails.

2.2 Deposition Simulation

The works cited thus far have all used either highly simplified deposition models, or models that are developed specifically for aerosol spray atomizers. Automotive coating processes are moving increasingly towards the use of electrostatic rotating bell (ESRB) atomizers in order to increase transfer efficiencies [14, 15, 16]. In an ESRB atomizer, paint fluid is forced onto the inner surface of a high speed rotating bell, which is maintained at a high voltage of 50-90 kV relative to the grounded surface being painted. Most modern systems use negative polarity at the bell [1]. Figure 2 shows a schematic of the atomizer configuration. The paint flow breaks up at the edge of the bell, forming a cloud of droplets, as it is expelled radially due to centrifugal force imparted to the paint by the rotating bell. Each paint droplet is charged due to the charge on the bell. If the particle charge is above the Rayleigh limit, the droplet will break apart, further atomizing the paint spray. High velocity shaping air, and often a charged pattern control ring, is used to force the charged particles towards the surface. Electrostatic forces and aerodynamic effects influence the trajectories of each particle.

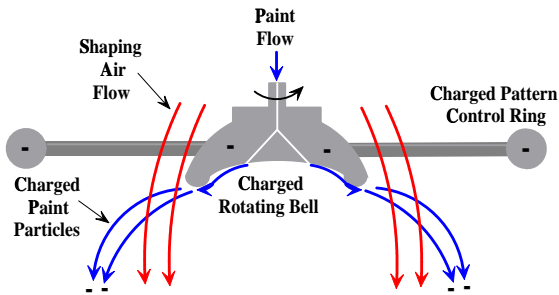


Figure 2: Electrostatic rotating bell atomizer with paint particle trajectory and shaping air flow lines shown.

Early work in modeling the electrical effects of these ESRB systems was performed by Elmoursi [15]. The simulation assumed a uniform droplet size and did not consider the evaporation of solvent during transport. Furthermore, neither aerodynamic effects nor the interdependence between the droplet trajectory and the electric field were taken into consideration. The model did consider the effect of space charge due to the distributed charged droplets on the electric field. Since the spatial charge distribution is dependent on the electric field, which is in turn dependent on the spatial charge distribution, an iterative solution technique was used to arrive at a mutually consistent solution. It was found that increasing the charge density of the particles increased the electric field, thereby increasing the deposition. However, there was a tradeoff in that increased charge densities increased the expansion of the spray cloud. For charge densities that were too low, the cloud did not expand, leaving a noticeable doughnut shape. High charge densities caused the outer portions of the fan to be exposed to weaker fields, thereby limiting the deposition. In addition to the voltage, the charge density is affected by the bell speed, paint delivery rate, and paint resistivity.

Ellwood and Braslaw developed a finite element model of the deposition characteristics of the ESRB atomizers, which extended the work of Elmoursi by including momentum effects [14]. The impact of various particle sizes was included by modeling a large number of trial trajectories for several particle size classes. Because the particle charging time scales are on the order of the time scale of the atomization process, the paint particles are often incompletely charged. The simulation used a constant charge-to-mass ratio, based on prior work in the literature. For each trial, the momentum balance on each particle was calculated based on the aerodynamic drag forces and electrostatic forces due to the charged particle moving through the electric

field. The model accounted for the exchange of momentum between the paint droplets and the gas phase due to solvent evaporation. The space charge density is calculated as an ensemble average of all of the trials over all size classes. A streamline, upwind, Petrov-Galerkin finite-element (SUPG) formulation is used to solve the coupled dynamic and electrical equations of the continuous gas phase and electrical field based on the discrete particle trajectories. The simulation then iteratively solves for the particle trajectories assuming an electric field, and the electric field assuming particle trajectories, until the solutions converge. Simulations with and without the pattern control ring were conducted. The pattern control ring exerts force onto the particles through an electric field sufficient to direct the spray plume towards the surface, thereby increasing the transfer efficiency of the process. One effect predicted by the simulation, and confirmed by experimental observation, is a double ring phenomenon in the deposition pattern, where the paint is deposited in two concentric rings.

Huang and Lai also conducted studies of the spray transport from the ESRB atomizer using finite element techniques [16]. Fewer details of their derivation are given in their preliminary paper, but according to the authors the simulations show “consistent trends with experimental observation.”

3 Deposition Modeling

The deposition model developed in this report has two primary purposes: *i*) to capture the structure of the deposition pattern for use by planning tools, and *ii*) to support simulations that accurately predict the results of specific atomizer trajectories. These two purposes lead to contradictory criteria for evaluating the model. First, the model must be accurate enough to capture the structure of the deposition and accurately predict the deposition on a variety of surface shapes. However, the model must be tractable from the perspective of the simulation and planning tools, since the model will be used by the planner.

Furthermore, it is desired that the model be of an analytic form that admits a closed form calculation of partial derivatives. This will enable analytic local optimization with respect to quality measures. The desire for simple, analytic models has led us to reject explicit finite-element computation of fluid dynamics and electro-static effects of the type presented in [14, 15]. Although these techniques may generate more accurate simulations of paint deposition, and can therefore be justified during a final path validation and refinement, the computational expense is not justified during preliminary development of the path planning tools. A discrete representation, which could model arbitrary distributions, was also considered before being rejected due to the desire for analytic representations.

The pattern of paint deposition, or film build, generated by ESRB atomizers is a function of the specific atomizer, process parameters, shape of the surface, and relative orientation of the atomizer to the surface. For the ABB Micro-Micro Bell Atomizer studied in this report, the overall shape of the deposition pattern is roughly circular when the bell is oriented normal to a flat panel and the atomizer is stationary. The paint deposition pattern gives the measured paint thickness over two dimensions; we refer to this as the *2D deposition pattern*. As the atomizer passes over the surface, the majority of the paint emitted by the atomizer is deposited on the surface, although some paint is entrained in the shaping air and lost. We refer to the paint thickness profile orthogonal to the direction of travel, which is equivalent to that obtained by integrating the 2D deposition model along the direction of travel, as the *1D collapse*. Figure 3 shows the relationship between the 2D deposition pattern and the resulting 1D thickness profile. Our approach has been to model the 2D deposition pattern and the 1D collapse separately because the integral of the 2D deposition pattern is not tractable.

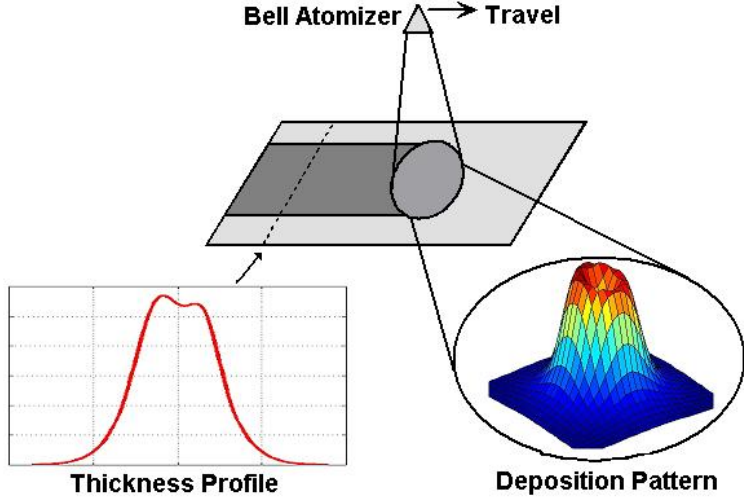


Figure 3: Painting flat panel showing the relationship between the 2D Deposition pattern and the integrated thickness profile (1D collapse).

3.1 2D Deposition Model

We were looking for a 2D deposition model that assigns the rate of paint deposition or *deposition flux* at a given point on an arbitrary surface, given a specific path location and orientation of the atomizer. The model we developed, denoted $D(\mathbf{s}, \mathbf{p})$, is of the form $D : \{\mathbb{R}^3 \times S^2\} \times SE(3) \rightarrow \mathbb{R}$, where $\mathbf{s} \in \mathbb{R}^3 \times S^2$ is a point and unit surface normal on the surface being painted and $\mathbf{p} \in SE(3)$ is a path location and orientation of the bell atomizer. We refer to $D(\mathbf{s}, \mathbf{p})$ as the *2D deposition model*, or simply the *deposition model*. The deposition model, which is dependent on the paint flow rate and other process parameters, is scaled to give the deposition flux. The total thickness at a given point on the surface is dependent on this deposition flux, the path followed by the atomizer over the surface, and the speed at which the path is traversed [10, 12, 13].

Since parameterizing the deposition model for arbitrary surfaces is difficult at best, and since experimental data for planar surfaces is readily available, we developed an analytic model for deposition flux on a planar surface. Through recourse to differential geometry, the planar deposition is mapped onto an arbitrary surface in a way that preserves the total paint volume. We refer to the analytic model for the planar surface as the *planar deposition model*. The planar surface is referred to as the *deposition model plane*, and is shown in Figure 4. The deposition model plane is oriented normal to the atomizer a fixed distance Ω_d from the atomizer path location \mathbf{p} along the atomizer normal \vec{z} . We assume that the path location \mathbf{p} is the tool center point frame (TCPF) specified by the planner, and used by the robot control program. The TCPF specifies both the location of the tool center point, and the orientation of the tool in space. Often, the TCPF is specified on the automotive surface and not on the paint atomizer at the end of the robot. We assume the paint is emitted from a theoretical emission point \mathbf{e} located along the atomizer normal at the distance Ω_e from the tool center point. The distance from the emission point to the deposition model plane is given by $\Omega = \Omega_d - \Omega_e$. Given the TCPF \mathbf{p} , Ω_d , and Ω_e the paint emission point and deposition model plane are uniquely specified.

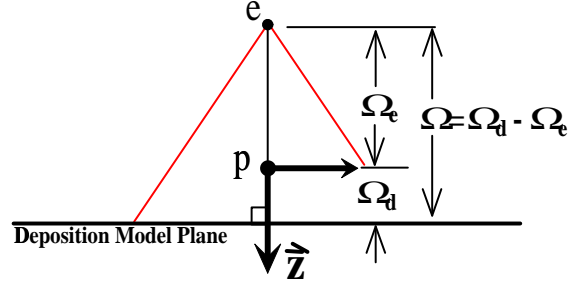


Figure 4: The atomizer path location uniquely determines both the emission point and deposition model plane. As drawn the value of Ω_e is negative since the emission point is behind the atomizer path location \mathbf{p} .

3.1.1 Planar Deposition Model

We denote the planar deposition model as $d(\mathbf{q}) = d(x, y)$, where $d : \mathbb{R}^2 \rightarrow \mathbb{R}$, and $\mathbf{q} = (x, y)$ is a point on the deposition model plane. The point \mathbf{q} is itself a function of the surface point \mathbf{s} and the atomizer path location \mathbf{p} , as shown in Figure 5. Because the emission point \mathbf{e} and the deposition model plane are directly related to the path location \mathbf{p} , the point \mathbf{q} is a function of both \mathbf{p} and \mathbf{s} , such that $d(\mathbf{q}) = d(\mathbf{q}(\mathbf{s}, \mathbf{p}))$. The orientation of the x-y deposition model plane about the z-axis of the bell atomizer is determined by the orientation of the atomizer assembly, and is independent of the direction of atomizer travel.

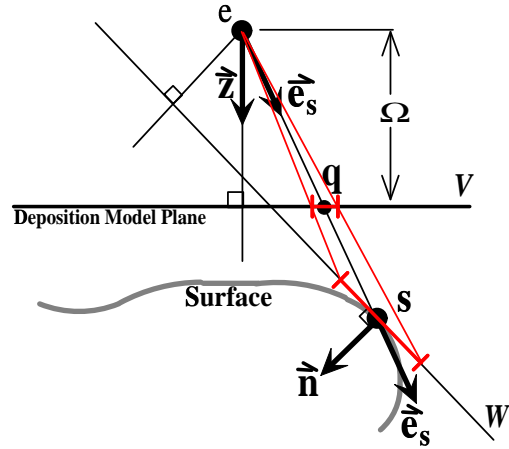


Figure 5: Projection of deposition model onto arbitrary surface. Although the vectors are in reality three dimensional, this simple figure conveys the basic results. (Note: The path location \mathbf{p} is not shown.)

The planar deposition model uses two Gaussians—one offset 1D Gaussian revolved around the origin and

one 2D centered Gaussian—and a scaling function that generates an asymmetry in the model. The asymmetry is required because significant asymmetry was found in preliminary experiments. Although the rotating bell is axially symmetric, the shaping air nozzles and pattern control ring are not necessarily symmetric, which give rise to the asymmetries found in the patterns [1]. The resulting planar deposition model, similar to the asymmetric volcano shown in Figure 3, is given by

$$d(x, y) = K_1 ((1 - K_2) f(x, y) g_1(x, y) + K_2 g_2(x, y)) , \quad (1)$$

where $K_1 \in \mathbb{R}^+$ scales the distribution to give the paint deposition flux in units of thickness per second and $K_2 \in [0, 1]$ weights the revolved Gaussian against the centered Gaussian. To account for asymmetry in the deposition pattern, the revolved offset Gaussian, $g_1 : \mathbb{R}^2 \rightarrow \mathbb{R}$, is scaled by the function $f : \mathbb{R}^2 \rightarrow \mathbb{R}$. We define f to be

$$f(x, y) = (1 + K_3 \sin(\text{atan2}(y, x) - \phi)) ,$$

where $K_3 \in [0, 1]$ weights the asymmetry scaling function for the revolved Gaussian¹. The phase angle, ϕ , allows the asymmetry to be localized relative to the atomizer reference frame.

Looking at the individual components of (1), the notion of revolving an offset Gaussian for g_1 is somewhat ambiguous. Figure 6 shows two possible choices. In the first the values for $x \in [0, \infty]$ are determined and then rotated about the vertical axis shown in the left figure. This yields the result shown by the lower curve in the figure on the right. The resulting swept volume is not differentiable at the origin. This is due to the lost “tail” to the left of the axis of rotation. The second choice is to account for the tail being swept along with the curve and adding to the result. This results in a differentiable function as shown by the upper curve in the right hand side of Figure 6. Using this technique, the revolved offset Gaussian, g_1 , is defined to be

$$g_1(x, y) = \frac{1}{\gamma} \left(\exp \left(-\frac{(\sqrt{x^2 + y^2} - r)^2}{2\sigma_1^2} \right) + \exp \left(-\frac{(\sqrt{x^2 + y^2} + r)^2}{2\sigma_1^2} \right) \right) ,$$

where r is the offset radius, σ_1 is the standard deviation of the Gaussian, and γ normalizes the deposition such that integral of g_1 over x and y equals one. The scaling factor γ is given by

$$\gamma = 2\pi \left(2\sigma_1^2 \exp \left(-\frac{r^2}{2\sigma_1^2} \right) + r\sigma_1\sqrt{2\pi} \operatorname{erf} \left(\frac{r}{\sqrt{2}\sigma_1} \right) \right) .$$

The second exponential in g_1 accounts for the “tail” of the Gaussian that crosses the axis of revolution.

The centered Gaussian, $g_2 : \mathbb{R}^2 \rightarrow \mathbb{R}$, also normalized, is given by

$$g_2(x, y) = \frac{1}{2\pi\sigma_2^2} \exp \left(-\frac{x^2 + y^2}{2\sigma_2^2} \right) ,$$

where σ_2 is the standard deviation of the centered Gaussian.

3.1.2 Surface Projection Model

The planar model defined above applies to deposition on flat panels, with the atomizer oriented normal to the surface and located a fixed offset distance from the deposition model plane. The next step in the

¹The scaling function has been modified based on the experimental results given in Section 4. The reader is referred to Appendix A for the definition of the latest model.

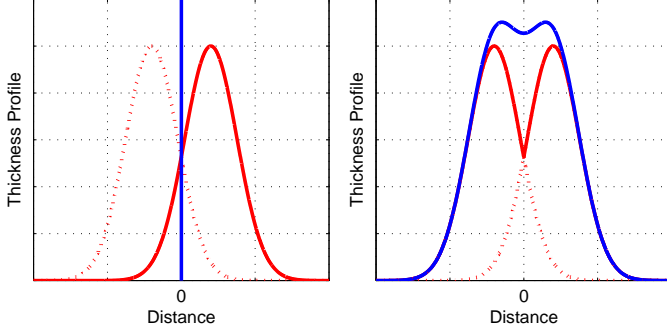


Figure 6: (l) Offset Gaussian bump shown with 180° rotation. (r) Curves showing result of considering the tail of the Gaussian in the revolved surface (upper) and ignoring the tail portion (lower).

model development is to extend the planar model to arbitrary surfaces, offset distances, and orientations. We simplify the model using a simple geometric projection, which ignores the electrostatic and fluid dynamic effects of the paint spray, just as in the prior work cited in Section 2. However, our derivation preserves the total paint volume [9, 10, 12]. We chose this projection model because typical car painting applications keep the bell atomizer at a roughly constant offset distance, and roughly normal orientation relative to the surface being painted.

The projection model, shown in Figure 5, is developed by assuming that all of the paint emits from a point source, called the emission point e , which is constrained to lie along the bell-to-surface vector \vec{z} as described above. Note, this emission point is a theoretical emission point, not necessarily coincident with the bell atomizer center point.

The deposition model plane is embedded in \mathbb{R}^3 orthogonal to the \vec{z} vector a distance Ω from the emission point. Furthermore, we assume that the x-y frame of the planar deposition model is aligned with the x-y plane of the atomizer reference frame. A vector from the emission point to a point s on the surface passes through the deposition model plane at point $q = q(s, p)$. We abuse notation and use q to refer to either the 2D position (x, y) on the deposition model plane or the 3D position (x, y, Ω) relative to the emission point. The point q is a function of both the path location and the surface point. It is assumed that the planar deposition $d(q) = d(x, y)$, as defined in (1), is known for a given point $q = (x, y, \Omega)$ on the deposition model plane defined in Figure 5.

A differential element on the deposition model plane gives a paint solids volume of $V = d(q) dx dy$. In the general case, as this differential element is projected onto the surface about point s , the area of the projection is different from that of the differential element. In order for the total volume, and therefore the total paint mass (assuming constant solids density), to remain unchanged, the paint thickness must change. We will derive the required relationship between the thickness on the planar model and the projected thickness on the surface using the concept of area magnification as defined in differential geometry [17].

We simplify the derivation by using two steps: first we map the deposition from the deposition model plane to the emission point in a way that preserves volume, then map from the emission point to the surface². Let $U_p = \{(\theta, \phi) \in]-\pi/2, \pi/2[\times]-\pi/2, \pi/2[\} \subset S^2$ – i.e., the open lower hemisphere centered at the

²The map is actually to a sphere with infinitesimal radius centered at the emission point.

emission point as determined by \mathbf{p} , the path location³. If we define $\theta = \text{atan2}(x, \Omega)$ and $\phi = \text{atan2}(y, \Omega)$, the point in the $U_{\mathbf{P}}$ parameter space corresponds to the unit vector $\vec{\mathbf{e}}_s$ shown in Figure 5. Let $V_{\mathbf{P}}$ be the deposition model plane embedded in \mathbb{R}^3 at $z = \Omega$. The mapping $\varphi : U_{\mathbf{P}} \rightarrow V_{\mathbf{P}}$ is given as

$$\varphi(\theta, \phi) = (\Omega \tan \theta, \Omega \tan \phi, \Omega). \quad (2)$$

For the map $\varphi : U_{\mathbf{P}} \rightarrow V_{\mathbf{P}}$ defined above, the coordinate vector fields are defined as $E_1 = \partial \varphi / \partial \theta = (\Omega \sec^2 \theta, 0, 0)$, $E_2 = \partial \varphi / \partial \phi = (0, \Omega \sec^2 \phi, 0)$, with normal orientation given by $\mathbf{N} = (0, 0, 1)$.

In order to conserve paint volume, the thickness must decrease as the area increases, and vice versa. This allows the calculation of the deposition in the $U_{\mathbf{P}}$ parameter space, $d_{U_{\mathbf{P}}}(\theta, \phi) : U_{\mathbf{P}} \rightarrow \mathbb{R}$, based on the planar deposition model for the deposition model plane and the area magnification factor of the map φ at point \mathbf{q} . The deposition in the $U_{\mathbf{P}}$ parameter space is given by

$$d_{U_{\mathbf{P}}}(\theta, \phi) = \text{AM}_q(\varphi) d(\mathbf{q}), \quad (3)$$

where the area magnification $\text{AM}_q(\varphi)$ is given by

$$\text{AM}_q(\varphi) = \det \begin{pmatrix} E_1 \\ E_2 \\ \mathbf{N} \end{pmatrix} = \Omega^2 \sec^2 \theta \sec^2 \phi. \quad (4)$$

Now consider the projection from the emission point to a point \mathbf{s} on the surface being painted. Let W_s be the tangent plane attached to the surface at point \mathbf{s} . This tangent plane is defined by the point \mathbf{s} and the surface normal vector $\vec{\mathbf{n}}$.

The mapping from $U_{\mathbf{P}}$ to the tangent plane W_s , denoted $\psi : U_{\mathbf{P}} \rightarrow W_s$, is given by

$$\psi(\theta, \phi) = M(\tan \theta, \tan \phi, 1), \quad (5)$$

where M is given by

$$M = \frac{L \langle \vec{\mathbf{e}}_s, \vec{\mathbf{n}} \rangle}{\langle (\tan \theta, \tan \phi, 1), \vec{\mathbf{n}} \rangle},$$

and $L = \|\vec{\mathbf{es}}\|$, $\vec{\mathbf{e}}_s$ is a unit vector from the emission point oriented toward the surface point \mathbf{s} , and $\vec{\mathbf{n}}$ is the surface normal at point \mathbf{s} . The value of M given above is found by realizing that $M(\tan \theta, \tan \phi, 1)$ and $L \vec{\mathbf{e}}_s$ both define the vector that locates the point \mathbf{s} in a coordinate system centered at the emission point, and therefore have the same projection orthogonal to W_s along $\vec{\mathbf{n}}$. The surface normal $\vec{\mathbf{n}}$ is assumed to point toward the “inside” of the surface being painted on the outside. After differentiating ψ , taking the determinant as in (4), and simplifying, the area magnification from $U_{\mathbf{P}}$ to W_s at point \mathbf{s} is given by

$$\text{AM}_s(\psi) = \frac{L^2 \langle \vec{\mathbf{e}}_s, \vec{\mathbf{z}} \rangle^3 \sec^2 \theta \sec^2 \phi}{\langle \vec{\mathbf{e}}_s, \vec{\mathbf{n}} \rangle}. \quad (6)$$

Finally, given the deposition in the $U_{\mathbf{P}}$ parameter space, we calculate the deposition at the point \mathbf{s} on the W_s plane, $d_{W_s}(\mathbf{s}) : U_{\mathbf{P}} \rightarrow W_s$, as

$$d_{U_{\mathbf{P}}}(\theta, \phi) = \text{AM}_s(\psi) d_{W_s}(\mathbf{s}).$$

³The bracket notation $[\cdot]$, $]\cdot[$, and $[\cdot[$ or $]\cdot]$ refer to closed, open, and half-open intervals respectively

Combining with (3), we have

$$d_{W_s}(\mathbf{s}) = \frac{\text{AM}_q(\varphi)}{\text{AM}_s(\psi)} d(\mathbf{q}) . \quad (7)$$

Given a path frame \mathbf{p} , a surface point \mathbf{s} , and the vectors \vec{z} and \vec{e}_s , the deposition model plane intersection point \mathbf{q} , and the surface normal \vec{n} at \mathbf{s} are all defined. Using (7), where the tangent plane W_s is used as a first order approximation of the surface at \mathbf{s} , we define the 2D deposition model for an arbitrary surface to be

$$D(\mathbf{s}, \mathbf{p}) = d_{W_s}(\mathbf{s}) = \frac{\Omega^2 \langle \vec{e}_s, \vec{n} \rangle}{L^2 \langle \vec{e}_s, \vec{z} \rangle^3} d(\mathbf{q}) , \quad (8)$$

where $d(\mathbf{q}) = d(\mathbf{q}(\mathbf{s}, \mathbf{p}))$ is the planar deposition model developed in Section 3.1.1, with $\vec{e}_s = \vec{e}_s(\mathbf{s}, \mathbf{p})$, $\vec{n} = \vec{n}(\mathbf{s})$, and $\vec{z} = \vec{z}(\mathbf{p})$.

3.2 1D Collapse Model

As the bell moves relative to the surface, the deposition pattern moves over the surface and paint is accumulated at each point on the surface. Since the deposition pattern is two dimensional, we refer to the result of integrating along the direction of travel as the *1D collapse* as mentioned earlier. The 1D collapse gives the film thickness profile as a function of distance perpendicular to the direction of travel, assuming that the deposition pattern does not vary with time or position along the surface. More formally, we will consider the deposition at a given point on the planar surface (x_0, y_0) , as the atomizer moves along normal to the surface over a period of time, as shown in Figure 7. The given point interacts with different locations in the deposition model as the pattern moves over the surface.

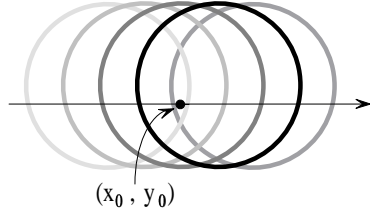


Figure 7: Schematic showing the interaction of different points on the deposition model as the pattern moves over a given point on the surface.

Without a loss of generality, let us assume that the deposition pattern is defined such that the direction of travel is along the y -axis of the atomizer and the deposition plane coincides with the planar surface. The total deposition, or *film build*, at (x_0, y_0) from a single pass of the atomizer is given by

$$T(x_0, y_0) = \int_{-t_{lim}}^{t_{lim}} d(x_0, y_0 + v_y t) dt , \quad (9)$$

where t_{lim} is the time at which the first or last paint is deposited at (x_0, y_0) , and v_y is the velocity in the direction of travel. Define $y_{lim} = v_y t_{lim}$, and note that $dy = v_y dt$. We may rewrite (9) as

$$T(x_0, y_0) = \int_{-y_{lim}}^{y_{lim}} d(x_0, y_0 + y) \frac{1}{v_y} dy , \text{ or}$$

$$T(x_0, y_0) = \frac{K_1}{v_y} \int_{-y_{lim}}^{y_{lim}} \left((1 - K_2) f(x_0, y_0 + y) g_1(x_0, y_0 + y) + K_2 g_2(x_0, y_0 + y) \right) dy. \quad (10)$$

Unfortunately, the complexity of the analytic model renders the calculation of an analytic integral for (10) intractable. Instead, we directly define a 1D collapse model using three separate Gaussians. In this model, chosen because it fit the experimental data well, two Gaussians are offset from the centerline to allow asymmetries in the deposition pattern to be modeled, while the third Gaussian is centered. The complete 1D collapse model is given by

$$c(x) = \frac{1}{3\sqrt{2}\pi} \left(\frac{1}{\sigma_1} \kappa_1 \exp\left(-\frac{(x-r_1)^2}{2\sigma_1^2}\right) + \frac{1}{\sigma_2} \kappa_2 \exp\left(-\frac{(x+r_2)^2}{2\sigma_2^2}\right) + \frac{1}{\sigma_3} \kappa_3 \exp\left(-\frac{x^2}{2\sigma_3^2}\right) \right). \quad (11)$$

The three exponential terms that constitute this model are each normalized, and r_i represents the offsets and σ_i the standard deviations. The gains κ_i are used to specify the paint deposition thickness for each Gaussian, and are different from the constants defined for the 2D deposition model. Figure 8 shows the component Gaussians and the composite film build for a particular set of parameter values for (11). Note this model assumes a particular direction of travel, and will most likely have different parameter values for different directions of travel. Experimental determination of the parameter values is discussed in Section 4.

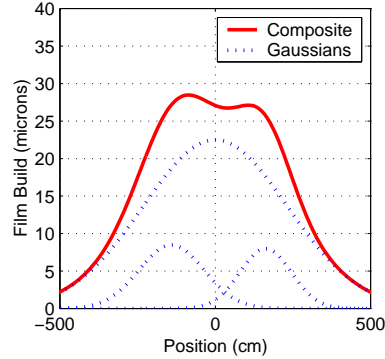


Figure 8: Asymmetric 1D collapse model with component Gaussians shown.

3.2.1 Planar Thickness Variation Calculation

In order to control the amount of variation in the coating thickness, the trajectory planner must know the relationship between the deposition pattern of the atomizer and the deposition on the surface being painted. For painting specialists, the knowledge is intuitive based on years of experience. To automate the process of generating these trajectories, we need a computable understanding of the relationship between deposition patterns and thickness variation.

Typically, the deposition pattern is narrow compared to the width of the surface being painted, and requires multiple passes to completely cover the surface as shown in Figure 9. The distance between consecutive passes is known as the *index distance*; the process of changing painting lanes is referred to as indexing. A natural question when planning paths for the painting robot is, ‘what is the appropriate index distance to control variation?’ Initially restricting ourselves to a flat panel, we will answer this question by looking at the paint deposition thickness profile perpendicular to the direction of travel using the 1D collapse model. We assume that the robot is moving in a straight line, and that the path is sufficiently long so that effects due to changing directions are negligible⁴.

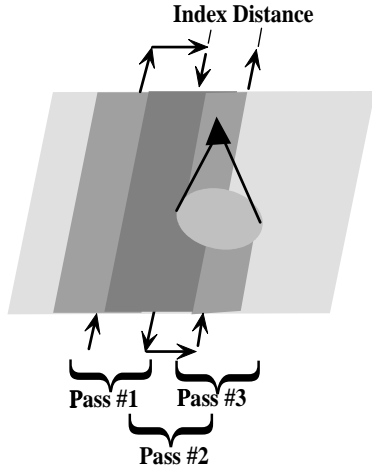


Figure 9: Painting a flat panel with 3 passes.

To develop an understanding of how the deposition pattern and index distance interact to determine thickness variation, we will assume an infinite plane painted by an infinite number of passes with the atomizer at a consistent orientation relative to the plane and moving at a constant speed. For a given location x in the interior of the plane, along a line perpendicular to the direction of travel, the total thickness is given by

$$T(x, \Delta x) = \sum_{i=-\infty}^{\infty} c(x + i \Delta x), \quad (12)$$

where Δx is the index distance, and $c(\cdot)$ is the 1D collapse model for the given speed and orientation relative to the direction of travel. In this case, the 0th pass is assumed to be along a centerline of the plane, with the variable x being measured relative to this centerline, perpendicular to the direction of travel. Looking at the thickness measurements as we vary x , the measurement pattern repeats itself with a period equal to the index distance.

The thickness variation, over one index distance, is given by

$$\sigma^2 = \frac{1}{\Delta x} \int_{-\frac{\Delta x}{2}}^{\frac{\Delta x}{2}} (T(x, \Delta x) - \bar{T})^2 dx, \quad (13)$$

⁴The question, ‘What is sufficiently long?’, is answered relative to the diameter of the deposition pattern.

where \bar{T} is the average thickness over the interval, which is defined as

$$\bar{T} = \frac{1}{\Delta x} \int_{-\frac{\Delta x}{2}}^{\frac{\Delta x}{2}} T(x) dx. \quad (14)$$

The limits of integration were chosen due to the periodicity of the variation calculation, but are otherwise arbitrary. For this reason, both the limits of integration and the $1/\Delta x$ term are considered to be constants.

The normalized variation over one index, with respect to the average thickness \bar{T} , is given by

$$\sigma_N^2 = \frac{1}{\Delta x} \int \left(\frac{T(x, \Delta x)}{\bar{T}(\Delta x)} - 1 \right)^2 dx = \Delta x \frac{\int T(x, \Delta x)^2 dx}{(\int T(x, \Delta x) dx)^2} - 1. \quad (15)$$

Note, the limits of integration have been dropped for compactness, but are the same as (14). The integral may be expanded, using equations (12) and (14), to give

$$\sigma_N^2 = \Delta x \frac{\sum_{i=-\infty}^{\infty} \sum_{j=-\infty}^{\infty} \int c(x + i \Delta x) c(x + j \Delta x) dx}{\sum_{i=-\infty}^{\infty} \sum_{j=-\infty}^{\infty} \int c(x + i \Delta x) dx \int c(x + j \Delta x) dx} - 1. \quad (16)$$

The integral terms in the denominator are tractable, and lead to terms involving the error function, $\text{erf}(\cdot)$. The result being given by

$$\int c(x + j \Delta x) dx = \sqrt{\frac{\pi}{2}} \left(\begin{array}{l} \sigma_1 \text{Erf}\left(\frac{x - r_1 + j \Delta x}{\sqrt{2} \sigma_1}\right) + \\ \sigma_2 \text{Erf}\left(\frac{x + r_2 + j \Delta x}{\sqrt{2} \sigma_2}\right) + \\ \sigma_3 \text{Erf}\left(\frac{x + j \Delta x}{\sqrt{2} \sigma_3}\right) \end{array} \right). \quad (17)$$

The integral term in the numerator results in a more complex solution, but an analytic solution does exist. The equations are sufficiently complex so that a numerical integration is warranted in the calculation of the numerator term in the summation. Numerical integration was used to generate the plots in this and the following sub-sections.

With regard to the infinite summations, the infinite extents of the Gaussian distributions used in the deposition models are an idealization. The actual deposition patterns are clearly finite, so the summations may be truncated based on the number of passes that interact with a given point on the surface. For simulation purposes, we chose to truncate the summations based on a 5σ calculation. Given the 1D collapse model, we calculate the interaction width as

$$W = \max(r_1 + 5\sigma_1, r_2 + 5\sigma_2, 5\sigma_3),$$

choosing the interaction width based on both the offset radius and the standard deviations. The summation limits, both positive and negative, are then calculated as

$$N = \text{ceiling} \left(\frac{W}{\Delta x} \right). \quad (18)$$

Using equations (16), (17), and (18), along with basic numeric integration, the variation as a function of the index distance for a given set of 1D collapse parameter values can be calculated.

A typical deviation, defined as the square root of variation, versus index distance curve is shown in Figure 10. As expected large indices yield high variation. If the model was only a single center Gaussian, the

variation versus index distance curve would be an isotone (monotonically increasing) function. However, in cases where there are significant offset Gaussian terms, there is a local minimum in variation versus index distance curve. The existence of this “sweet spot” may allow the use of larger index distances to generate paint coverage with acceptable variation, while reducing total cycle time. However the variation tends to be sensitive to changes in index distance at this spot, so for tight tolerances, keeping index distances smaller than the local minimum may be advisable. Knowledge of how the thickness variation changes with changes in index distance is helpful to the trajectory planner, whether in determining an absolute index distance or in evaluating the sensitivity of a given index distance.

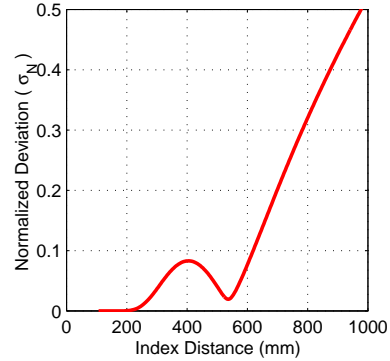


Figure 10: Normalized deviation vs. index distance for a typical 1D collapse model on a flat surface.

The ability to evaluate the thickness variation as a function of model parameter values, as well as atomizer orientation and surface effects, allows us to analyze the effects of changes on any of these operational variables. For example, consider the effect of changing the offset distance, which impacts the 1D collapse parameter values. Figure 11 shows the variation surface generated by varying both the index distance and the offset distance. The closed form solutions given above allow us to analyze the effect on coating thickness from varying any of the parameter values.

With the analytic representation for variation given in (16), we are able to evaluate the structural effects of a given model on variation as we vary the index distances. By evaluating the partial derivative with respect to index distance, we can employ root finding techniques to find local minimum of the variation. We begin by taking the partial derivative of (15) to give

$$\begin{aligned} \frac{\partial \sigma_N^2}{\partial \Delta x} &= 2\Delta x \frac{\int T(x, \Delta x) \frac{\partial T(x, \Delta x)}{\partial \Delta x} dx}{\left(\int T(x, \Delta x) dx\right)^2} \\ &\quad - 2\Delta x \frac{\int T(x, \Delta x)^2 dx}{\left(\int T(x, \Delta x) dx\right)^3} \int \frac{\partial T(x, \Delta x)}{\partial \Delta x} dx. \end{aligned} \quad (19)$$

Because the Δx term in front of (16) and the limits of integration are arbitrarily chosen to be equal to the index distance, they are considered to be constants with respect to the partial differential calculation, and do not yield additional terms in the partial calculation.

Define $c_i(\Delta x) = c(x + i\Delta x)$, where $c_i(\cdot)$ is the 1D collapse function and the subscript i denotes the index variable used in summation terms. Expanding (19), and using the linearity of both the integral and

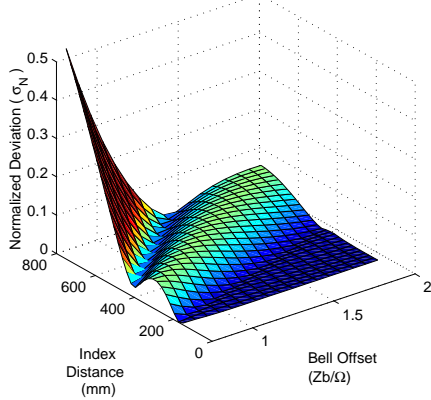


Figure 11: Normalized deviation vs. index distance and offset distance for a typical deposition model on a flat surface. Z_b is the actual offset distance from the surface to emission point, while Ω is the nominal offset distance to the deposition model plane.

partial differentiation operators, we obtain

$$\begin{aligned} \frac{\partial \sigma_N^2}{\partial \Delta x} &= 2 \Delta x \frac{\sum_i \sum_j \int \left(c_i(\Delta x) \frac{\partial c_j(\Delta x)}{\partial \Delta x} \right) dx}{\sum_i \sum_j \int c_i(\Delta x) dx \int c_j(\Delta x) dx} \\ &\quad - 2 \Delta x \frac{\sum_i \sum_j \sum_k \int (c_i(\Delta x) c_j(\Delta x)) dx \int \frac{\partial c_k(\Delta x)}{\partial \Delta x} dx}{\sum_i \sum_j \sum_k \int c_i(\Delta x) dx \int c_j(\Delta x) dx \int c_k(\Delta x) dx}. \end{aligned} \quad (20)$$

The summations are between negative and positive N , as defined in (18). Looking at each integral term, first note that

$$\frac{\partial c_j(\Delta x)}{\partial \Delta x} = j \frac{\partial c_j(\Delta x)}{\partial x},$$

which implies that

$$\int \frac{\partial c_j(\Delta x)}{\partial \Delta x} dx = j c_j(\Delta x).$$

The term

$$\int c_i(\Delta x) \frac{\partial c_j(\Delta x)}{\partial \Delta x} dx$$

does not have an analytic solution (at least none solvable by MathematicaTM), but can easily be solved by numeric integration. The term

$$\int c_i(\Delta x) c_j(\Delta x) dx$$

has an analytic solution, but as mentioned before, the solution is so complicated that numeric integration is also advised. Because of the linearity, the summation terms can be moved inside the integral to improve the efficiency of the overall numeric solution. Denoting numeric integration by “Int()”, and making the

substitutions given above, we can rewrite (20) as

$$\begin{aligned} \frac{\partial \sigma_N^2}{\partial \Delta x} &= 2\Delta x \frac{\text{Int}\left(\sum_i \sum_j c_i(\Delta x) \frac{\partial c_j(\Delta x)}{\partial \Delta x}\right)}{\sum_i \sum_j \int c_i(\Delta x) dx \int c_j(\Delta x) dx} \\ &\quad - 2\Delta x \frac{\text{Int}\left(\sum_i \sum_j c_i(\Delta x) c_j(\Delta x)\right) \sum_k k c_k(\Delta x)}{\sum_i \sum_j \int c_i(\Delta x) dx \int c_j(\Delta x) dx \int c_j(\Delta x) dx}, \end{aligned} \quad (21)$$

where the integral terms in the denominators are evaluated according to (17).

3.2.2 Cylindrical Thickness Variation Calculation

The development of the above variation calculations was presented for planar surfaces. To calculate the variation on the surface of a cylinder, one might imagine taking the planar 1D collapse, and projecting it around the cylinder. This does not work due to the distortion of the deposition pattern as it is projected onto the curved surface of the cylinder, as well as paint lost due to overspray. Our approach will be to first calculate the 2D deposition on the cylinder using the 2D deposition model developed in Section 3.1, and then calculate the 1D collapse of the deposition on the cylinder. We can numerically integrate (8) to find numeric values for the paint thickness profile on the cylinder orthogonal to the direction of travel. There are two primary directions to travel: either around the cylinder and index along the cylinder, or along the cylinder indexing around the cylinder as shown in Figure 12

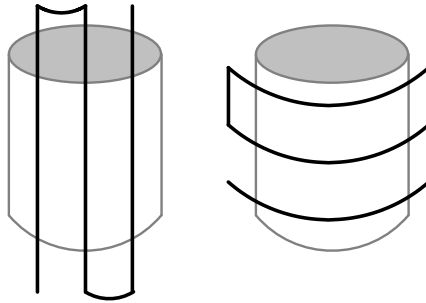


Figure 12: (l)Painting along the cylinder axis, and indexing around the cylinder. (r) Painting around the cylinder, and indexing along the cylinder axis.

Consider the arrangement shown in Figure 13, where we are painting the outside of a cylinder. The cylinder is centered along the y-axis, with $x^2 + z^2 = R_c^2$, where R_c is the radius of the cylinder. We assume that the paint atomizer is oriented normal to the surface, located along the y-axis at an angle θ from the x-axis in the xz-plane. Specifying the atomizer path location as $(R_b \cos \theta, y_b, R_b \sin \theta)$, where the radius of the path location is defined to be $R_b = R_c + \Omega_d$, the orientation of the atomizer frame is given as $(-\cos \theta, 0, -\sin \theta)$. We refer to a point s on the surface as being located at $(R_c \cos \Psi, y_s, R_c \sin \Psi)$, with an inward pointing normal of $(-\cos \Psi, 0, -\sin \Psi)$.

When painting a cylinder, the radius of the cylinder has a direct impact on the deposition of paint on the surface. This is due to both the curvature effects and the paint lost due to over spray. Smaller cylinder radii result in more paint loss, as depicted in Figure 14. Note, that our geometric projection model precludes

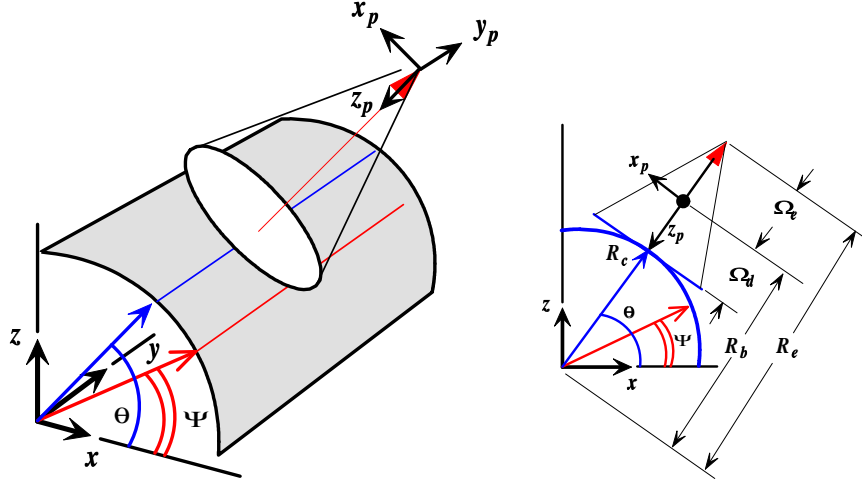


Figure 13: Painting a cylindrical surface. The atomizer location is specified by the model parameters, the angle θ , and the distance along the cylinder axis y_b . A point on the cylinder surface is specified by the angle Ψ and the distance along the cylinder axis y_s .

painting more than a 180 degree arc of the cylinder. The actual limitation can be calculated given the radius of the cylinder R_c and the location of the emission point, $R_e = R_b - \Omega_e$, where R_b is the radius of the path location and Ω_e is the distance from the path location to the emission point along the atomizer normal. At the limit, the angle between the vector from the emission point to a given surface point, and the surface normal vector is 90 degrees, as depicted in Figure 14. The limiting angle is given by

$$\Psi_{limit} = \cos^{-1} \frac{R_c}{R_e}.$$

When traveling around the cylinder, we will assume that we are painting a half cylinder, and that the indexing occurs on the back side of the cylinder. In this way paint does not fall on the half cylinder we are painting (due to the geometric projection), and indexing effects are negligible. The 1D collapse is calculated by integrating around the cylinder, from $-\Psi_{limit}$ to $+\Psi_{limit}$, creating a profile along the extrusion axis of the cylinder. Figure 15 shows the resulting 1D collapse profiles for a series of cylinder radii. Given the 1D collapse on the cylinder, the variation calculations are identical to the planar case when indexing along the cylinder axis of extrusion. Figure 16 shows the resulting thickness deviation surface as both cylinder radius and index distance are varied.

When traveling along the cylinder axis, the 1D collapse is calculated by integrating along the cylinder axis, resulting in a profile on a circular slice of the cylinder. We assume that indexing around the cylinder occurs at a distance away from where we measure the thickness profile, so that the indexing operation does not impact the thickness profile. Figure 18 shows the resulting 1D collapse profiles for various cylinder radii.

The 1D collapse thickness values are found by numerically integrating the deposition as projected onto cylinders of various radii. Unfortunately, for small cylinder radii the 1D collapse model developed in Section 3.2 does not provide a good model to the numerically obtained data. In other words, the best parameter fit for

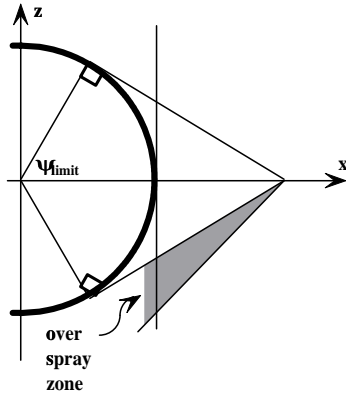


Figure 14: Lost paint due to over spray, assuming geometric projection.

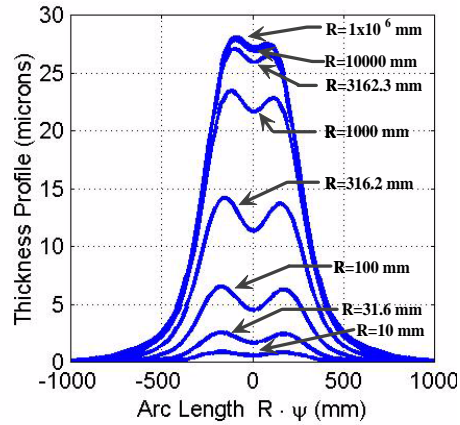


Figure 15: 1D collapse thickness profiles, obtained by integrating the deposition model after projection onto the cylinder, where the atomizer is painting around the cylinder and indexing along the axis of extrusion. The graphic also shows the results for a series of cylinders with radii of $R_c = 1 \times 10^6, 1 \times 10^5, 10000, 3160, 1000, 316, 100, 31.6$, and 10 mm. The thickness profile corresponding to the largest radius closely matches that of the flat panel profile. The thickness decreases as the radii decrease because of the increasing amount of paint lost to over spray due to the geometric projection developed in Section 3.1.2. The profile does maintain the basic shape even as the thickness decreases.

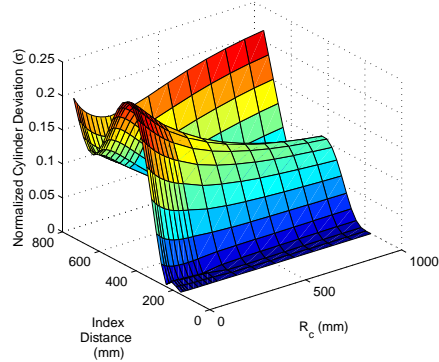


Figure 16: Normalized thickness deviation as a function of both cylinder radius and index distance when painting around the cylinder and indexing along the cylinder. As it moves, the atomizer is always oriented normal to the cylinder surface, at a constant offset.

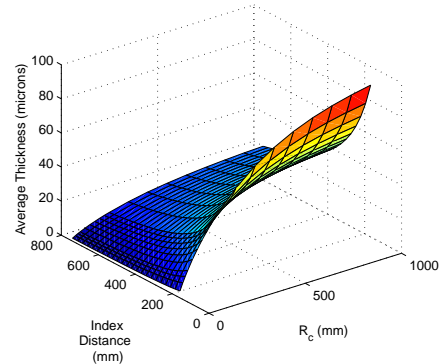


Figure 17: Average thickness values for cylinder painting corresponding to Figure 16.

(11) does not provide a good match to the data, as shown in Figure 19. One could define a new 1D collapse for this special case or solve the variation calculations numerically using the 2D model. Since the current 1D collapse fits well until the cylinder radii is much smaller than the deposition pattern width, we will not seek to define a new model at this time. Solving the variation calculations using numeric integration of the 2D deposition model is not used due to the computational inefficiencies involved. For these reasons, we will keep the current 1D collapse, and focus on cylinders with larger radii. It is expected that for the surfaces of interest, namely automotive surfaces, small radii of curvature will occur as character lines on larger less curved surfaces, which will dominate the planning. Once the 1D collapse is found, the variation calculations are identical with the index distance assumed to be arc length on the cylinder surface. The corresponding deviation surface is shown in Figure 20.

So far we have focused on painting the external (convex) surface of cylinders; we now switch to painting the inside (concave) surface of a cylinder as shown in Figure 21. We will restrict the discussion to cylinders

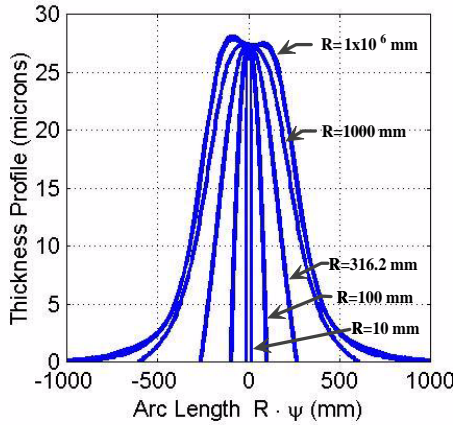


Figure 18: 1D collapse thickness profiles when painting along the cylinder axis of extrusion and indexing around the cylinder. The graphic also shows the results for a series of cylinders with radii of $R_c = 1 \times 10^6, 1000, 316, 100$, and 10 mm. The maximum thickness does not change significantly, but the profile gets thinner as the cylinder radius decreases.

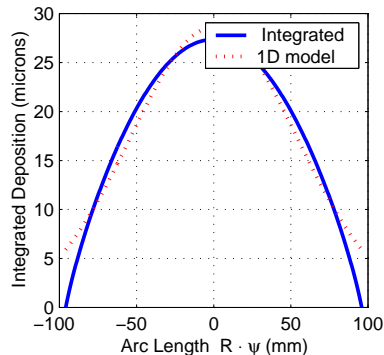


Figure 19: Attempted fit of 1D collapse model to the numerically integrated collapse when painting along the cylinder axis of extrusion for $R_c = 100$ mm. For the deposition parameter values used in these tests, the current 1D collapse model provides a good fit if the cylinder radius is 500 mm or greater.

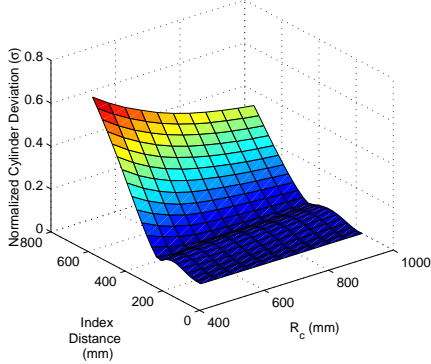


Figure 20: Normalized thickness deviation as a function of both cylinder radius and index distance when painting along the cylinder axis of extrusion and indexing around the cylinder. As it moves, the atomizer is always oriented normal to the cylinder surface, at a constant offset.

whose radii exceed the offset distance of the atomizer emission point from the surface, otherwise the emission point is beyond the surface focal point and indexing is ill defined. Note that all of the paint sprayed on the inside will fall on the surface, unlike the convex surface where paint is lost due to over spray. The actual calculations of deposition and variation are identical to convex painting, only the definition of the surface normals change.

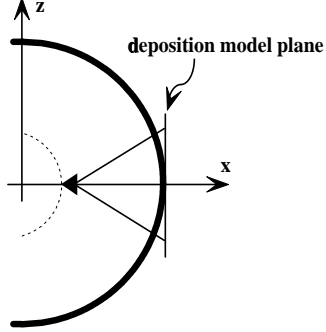


Figure 21: Painting the inside (concave) surface of a cylinder. We assume that the radius of the cylinder is larger than the offset of the atomizer emission point from the surface.

When painting around the inside of the cylinder, the deposition profile gets taller and sharper as the radius decreases, as shown in Figure 22. When painting along the inside of the cylinder, smaller radii tend to magnify the peaks due to the offset Gaussian terms, as shown in Figure 23. The 1D collapse model generally provides a good fit to the integrated collapse for cylinders with radii larger than the surface offset distance, whether painting along or around the cylinder.

While the preceding results on cylindrical surfaces are not directly applicable to automotive surfaces,

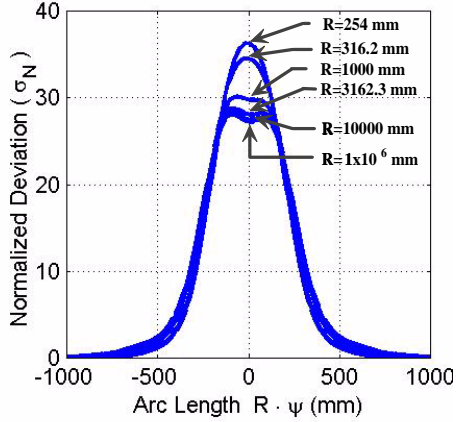


Figure 22: Integrated 1D thickness profiles for painting around the inside of a cylinder, and indexing along the cylinder. The graphic shows the results for a series of cylinders with radii of $R_c = 1 \times 10^6, 1 \times 10^5, 10000, 3162, 1000, 316.2$, and 254 mm. Notice, that when painting the inside of the cylinder, the radius changes have the opposite effect relative to painting the outside. Decreasing cylinder radius results in a thicker, sharper thickness profile.

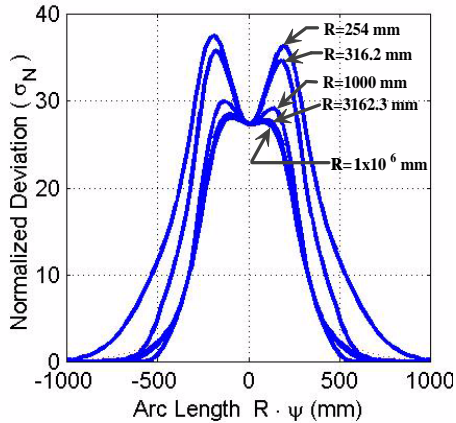


Figure 23: Integrated 1D thickness profiles for painting the inside surface of a cylinder along the axis of extrusion, and indexing around the cylinder. The graphic shows the results for a series of cylinders with radii of $R_c = 1 \times 10^6, 3162, 1000, 316.2$, and 254 mm. In this case, decreasing the cylinder radius amplifies the asymmetries present in the model.

they do provide insight into the relationship between the deposition pattern and the surface curvature. Our subsequent work will focus on more general “automotive-like” surfaces. In Section 4, we focus on results of experiments designed to evaluate our models and the theoretical results presented in this section.

4 Experimental Validation

The 2D deposition and 1D collapse models were validated by conducting a series of tests at ABB Process Automation in Auburn Hills, Michigan on September 26-27, 2001. The experiments used an ABB S3 robot with an ABB 50 mm Micro-Micro Bell atomizer attached to apply a solvent based automotive paint to phosphate coated test panels. The operating conditions of the application process were 80-90 kV electrostatic voltage, 150 cc/min paint flow, 250 l/min shaping air flow, and a bell speed of 30 000 RPM. The total film thickness of the oven cured test panels was measured with an Elcometer 355 coating thickness measuring device. Five measurements were taken for each data point, with the low and high discarded and the average of the remaining three recorded. The average phosphate thickness was then subtracted from the total film thickness to give the paint thickness.

4.1 Deposition Model Parameterization

In order to parameterize the 1D collapse and 2D deposition models, experimental data was gathered from flat panels painted by three passes as shown in Figure 5. Three different indices were tested: 525 mm, 577 mm, and 625 mm. We chose to parameterize our models using a 577 mm index distance for this three pass test because the observed variation was sufficient to discern the structural effects of the offset radii needed for the model parameterization. Figure 24 shows the steps that we followed. Using the 577 mm index test data, we used a standard numeric optimization routine in MATLABTM to determine the best parameter values $(\kappa_1, \kappa_2, \kappa_3, r_1, r_2, \sigma_1, \sigma_2, \sigma_3)$ for the 1D collapse model defined in (11). The maximum of the two offset radii and the maximum standard deviation from the 1D collapse model were then used to initialize the optimization of the 2D deposition model parameter values.

Given an initial parameterization of the 2D deposition model, we calculated the 1D collapse thickness values for the parameterized 2D model using numeric integration. The integrated 1D collapse values were then compared to the experimental data. Numeric optimization was used to find the 2D deposition model parameter values $(K_1, K_2, K_3, \phi, r, \sigma_1, \sigma_2)$ that minimized the sum squared error between the experimental data and the numerically integrated 1D collapse. The parameterized models, both 2D and 1D collapse, were shown previously in Figure 3. Figure 25 shows the resulting profile (1D collapse) obtained from a simulation using the 2D deposition model against the data to which it was fit. The simulation results were obtained through numeric evaluation of our deposition models, and match the experimental data well.

4.2 Planar Deposition Results

Using the 2D deposition model parameterized by the 577 mm index three pass test, the depositions generated by 525 and 625 mm index tests were simulated. The results are shown in Figure 26. The model gives a good prediction of both average film build and the structure of the variation for these flat panel tests. Most importantly, the model captured both the asymmetries and the structural variation dependence on index distance.

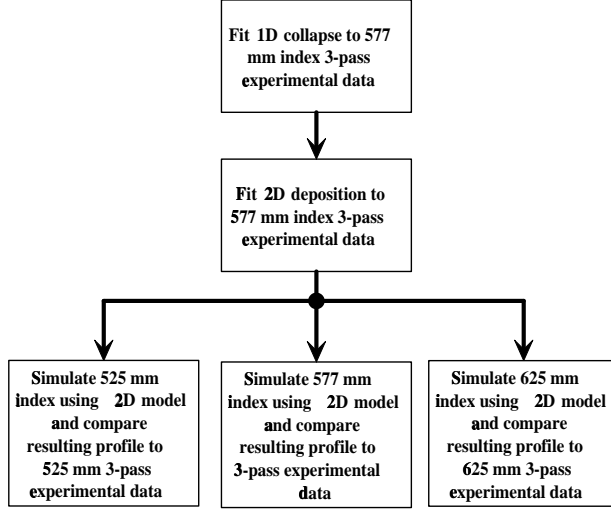


Figure 24: Steps in fitting and verifying model performance.

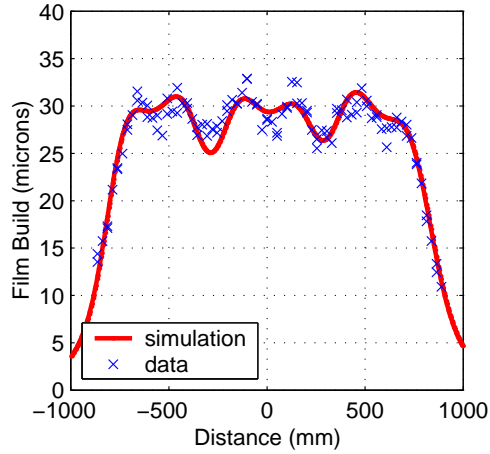


Figure 25: Flat panel test results using a 577 mm index distance (avg. error = -0.12 microns, standard deviation = 1.31 microns). The deposition simulation uses triangulated surface elements to model the thickness deposition at a given point on the surface.

4.3 Surface Deposition Results

Given the relatively good results of the flat panel tests, the projection of the planar deposition model onto arbitrary surfaces was tested. A representative automotive surface was obtained by using a truck door. Figure 27 shows a CAD model of the truck door used, with an example path shown. The door has a line of convex

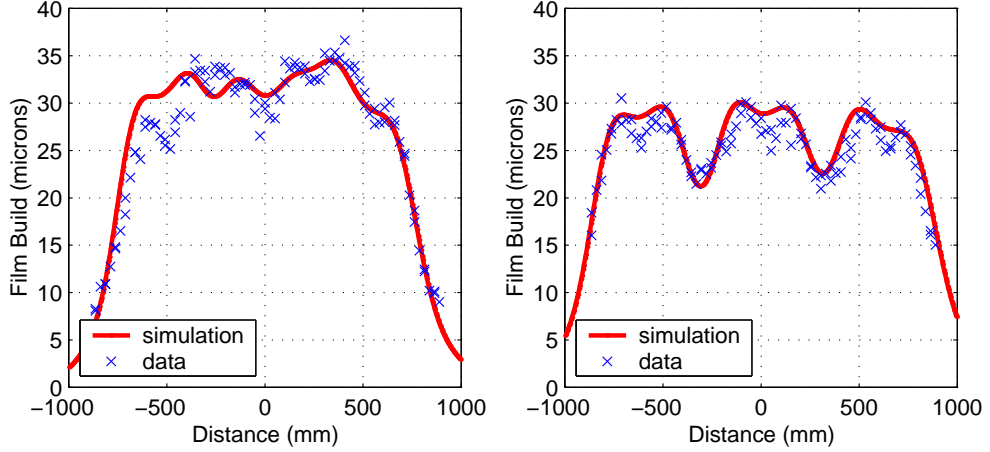


Figure 26: Flat panel test results: (l) 525 mm index test, and (r) 625 mm index test. Both (l) and (r) used the model parameterized by the data from the 577 mm index test. Both simulations capture the variation due to the structure of the deposition pattern. (average error: l = -0.69 and r = -1.05 microns, standard deviations: l = 2.41 and r = 1.68 microns).

curvature near the middle, with a pronounced concave curvature on the bottom third of the door. A series of tests were conducted using both horizontal and vertical passes over the door. For the horizontal passes, film build measurements were taken in four vertical columns of data spread across the door, numbered top to bottom. For the vertical passes, the measurements were taken from six rows spread vertically over the door spanning left to right across the door. For the first horizontal test, results for a typical column are shown in Figure 27. The simulated deposition for each pass individually is also shown.

Near the top of the door, in the relatively flat portion, the simulation gives somewhat reasonable results. However, the simulation has difficulty predicting paint thickness in the highly curved section near the bottom of the door. Clearly the pass along the lower portion of the door deposits more paint than the simulation predicts. It is theorized, as shown in Figure 28, that when the surface curves away from the atomizer, electrostatic effects dominate invalidating the geometric projection model described in Section 3.

Similar tests were conducted for vertical painting motions, with comparable results. For data collected on the upper relatively flat portion of the door, the simulation results were reasonable. However, for results on the lower portion of the door, the simulation again predicted too little paint deposition.

4.4 Miscellaneous Results

It was also desired to verify that our deposition models scale with applicator speed. To this end, two additional tests were conducted. These tests used a single pass, with the robot painting horizontally, at tip speeds of 100 mm/sec and 250 mm/sec. It was intended to compare these results to the 50 mm/sec 3-pass results. The 250 mm/sec test resulted in significant spattering at the nominal paint flow rates being used. Since the sensor was not designed to measure discrete drops of paint, the results were deemed inadmissible. The result for the 100 mm/sec test is shown in Figure 30. As shown, the simulation predicted much greater paint deposition than actually measured. It has been theorized that the transfer efficiencies increase when painting wet surfaces,

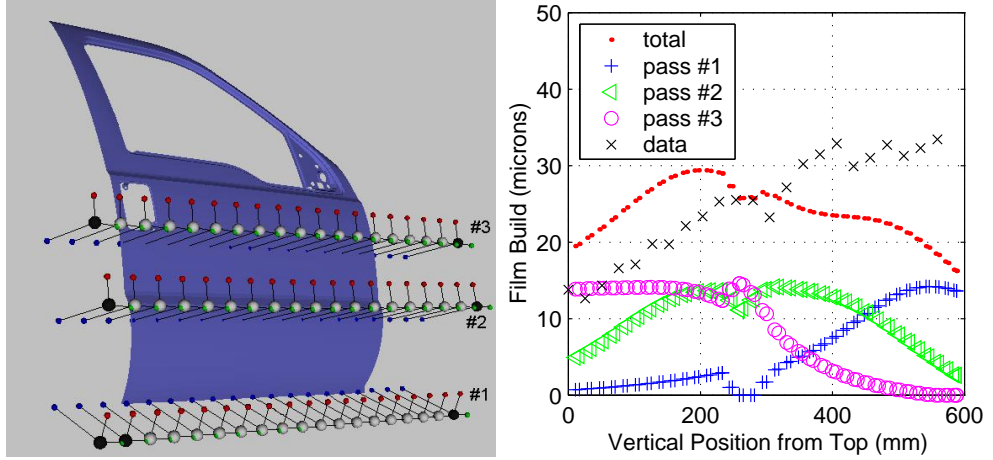


Figure 27: (l) Door with horizontal paint path shown. The robot paints left to right starting at the left of pass #1, then travels right to left along pass #2, finishing by going left to right along pass #3. (r) Simulation of a horizontal painting motion over the door, with deposition by individual passes shown.

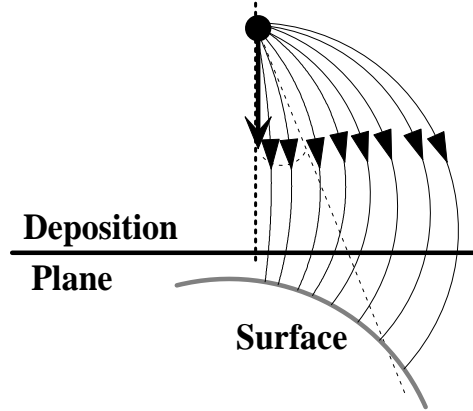


Figure 28: Theorized warping of paint particle trajectories due to electrostatic effects.

because some paint initially bounces off of the dry surfaces. Slower tip speeds allow more wet paint film to build up, thereby increasing the average transfer efficiency [1, 18].

Also notice that the data set in Figure 30 exhibits an asymmetry, while the simulation does not. During this test, the orientation of the atomizer was consistent with the previous 577 3-pass test, while the direction of travel was orthogonal to the 577 mm index test used in the model parameterization. The deposition model developed in Section 3 has a hemispheric asymmetry. This test implies the need for a more localized asymmetry term in the 2D model, as is defined in Appendix A. Since the 1D collapse model is dependent

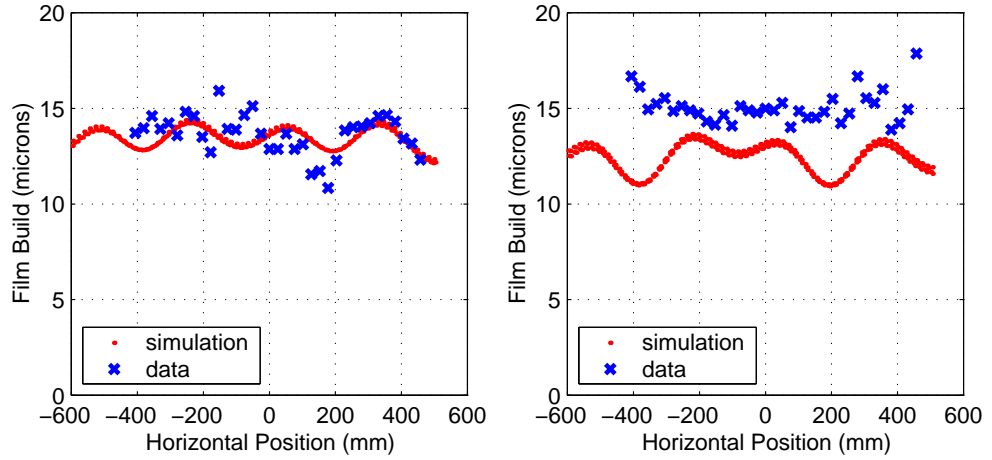


Figure 29: Vertical painting motion on door: (a) upper flat portion (b) lower curved portion

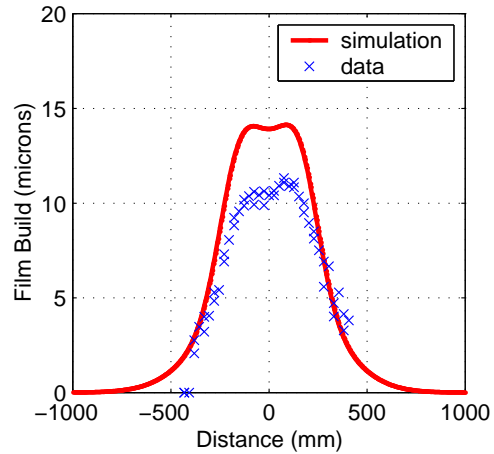


Figure 30: Single Horizontal pass with $V=100$ mm/sec. Simulation predicts higher paint deposition than data shows for this higher speed, likely due to changes in wet/dry transfer efficiency.

on the direction of travel anyway, no change to the 1D collapse model is needed. With the addition of this more localized asymmetry component, the model error would need to be calculated against both horizontal and vertical motions during the parameter optimization.

5 Conclusions

The results of our experimental study allow us to conclude that our models capture the relevant structure of the planar deposition pattern, and the dependence of the thickness variation on that structure. It is also apparent that the interaction of the paint droplets emitted from the atomizer and the surface curvature has a significant impact on the actual deposition pattern on curved surfaces. These preliminary conclusions also indicate the need for additional tests regarding the dependence of the deposition pattern and transfer efficiency on the speed of the atomizer as it moves relative to the surface.

The models we developed accurately predict deposition on planar surfaces, where the atomizer is oriented normal to the surface. Additionally, our analytic 1D collapse model effectively predicts the dependence of the thickness variation on the index distance between passes. Although the experimental results from deposition on the curved surface of the door point to shortcomings with the simple geometric projection developed in Section 3, the experiments do confirm the interaction of the surface curvature with the planar deposition pattern.

Despite the shortcomings of our 2D deposition model, the models are useful for our research. By using an analytic model, we are able to develop our understanding of the interaction between the surface, the deposition pattern, and the atomizer path. This enables our exploration of path planning techniques that influence overall quality measures such as thickness variation, cycle time, and efficiency. Since the main focus of our research is on path planning, we will continue to use these analytic models during the development phase of our planning tools. Since our planning tools rely only on the structure of the deposition on the surface, and not on the underlying model, the need for more expensive models or experimental data is delayed until the implementation stage.

During our next round of experiments, we will validate the modifications to the asymmetry terms in our planar deposition model. This will require three pass tests in both the horizontal and vertical directions, with the resulting model fit from the combination of both data sets. Experiments will be conducted to more rigorously evaluate the dependence of the deposition rate on the speed of the atomizer. For this we will need to differentiate between effects due to speed alone, and effects due to a prior build up of wet paint on the surface. We will also begin the preliminary validation of some of our path planning techniques with respect to openings in the surface and surface curvature.

6 Acknowledgments

This work was supported by the National Science Foundation through grant IIS-9987972 and the Ford Motor Company.

The authors gratefully acknowledge the assistance of the Ford Motor Company and ABB Process Automation for their assistance in conducting these experiments. We would like to specifically acknowledge Dr. Jake Braslaw, our Ford collaborator, who has been extremely helpful throughout this effort.

References

- [1] Jacob Braslaw. personal communication, 2001.
- [2] Ercan U. Acar, Howie Choset, Alfred A. Rizzi, Prasad N. Atkar, and Douglas Hull. Exact Cellular Decompositions in Terms of Critical Points of Morse Functions for Sensor-based Coverage Tasks. *The International Journal of Robotics Research*, accepted for publication 2001.
- [3] Ercan U. Acar and Howie Choset. Sensor-based Coverage of Unknown Environments: Incremental Construction of Exact Cellular Decompositions in Terms of Critical Points of Morse Functions. *The International Journal of Robotics Research*, accepted for publication 2001.
- [4] Prasad N. Atkar, Howie Choset, Alfred A. Rizzi, and Ercan U. Acar. Exact Cellular Decomposition of Closed Orientable Surfaces Embedded in \mathbb{R}^3 . In *IEEE Int'l. Conf. on Robotics and Automation*, Seoul, Korea, May 2001.
- [5] Suk-Hwan Suh, In-Kee Woo, and Sung-Kee Noh. Development of An Automated Trajectory Planning System (ATPS) for Spray Painting Robots. In *IEEE Int'l. Conf. on Robotics and Automation*, Sacramento, California, USA, April 1991.
- [6] Naoki Asakawa and Yoshimi Takeuchi. Teachless Spray-Painting of Sculptured Surface by an Industrial Robot. In *IEEE Int'l. Conf. on Robotics and Automation*, Albuquerque, New Mexico, USA, April 1997.
- [7] Eckhard Freund, Dirk Rokossa, and Jürgen Roßmann. Process-Oriented Approach to an Efficient Off-line Programming of Industrial Robots. In *IECON '98: Proceedings of the 24th Annual Conference of the IEEE Industrial Electronics Society*, volume 1, 1998.
- [8] Weihua Sheng, Ning Xi, Mumin Song, Yifan Chen, and Perry MacNeille. Automated CAD-Guided Robot Path Planning for Spray Painting of Compound Surfaces. In *IEEE/RSJ Int'l. Conf. on Intelligent Robots and Systems*, 2000.
- [9] Heping Chen, Weihua Sheng, Ning Xi, Mumin Song, and Yifan Chen. Automated Robot Trajectory Planning for Spray Painting of Free-Form Surfaces in Automotive Manufacturing. In *IEEE Int'l. Conf. on Robotics and Automation*, Washington, D.C., USA, May 2002.
- [10] M. A. Sahir and Tuna Balkan. Process Modeling, Simulation, and Paint Thickness Measurement for Robotic Spray Painting. *Journal of Robotic Systems*, Vol. 17(9), 2000.
- [11] Andreas Pichler, Markus Vincze, Henrik Anderson, Ole Madsen, and Kurt Häusler. A Method for Automatic Spray Painting of Unknown Parts. In *IEEE Int'l. Conf. on Robotics and Automation*, Washington, D.C., USA, May 2002.
- [12] Peter Hertling, Lars Høg, Rune Larsen, John W. Perram, and Henrik Gordon Petersen. Task Curve Planning for Painting Robots — Part I: Process Modeling and Calibration. *IEEE Transactions on Robotics and Automation*, Vol. 12(2), April 1996.
- [13] Ramanujam Ramabhadran and John K. Antonio. Fast Solution Techniques for a Class of Optimal Trajectory Planning Problems with Applications to Automated Spray Coating. *IEEE Transactions on Robotics and Automation*, Vol. 13(4), August 1997.

- [14] Kevin R. J. Ellwood and J. Braslaw. A Finite-Element Model for an Electrostatic Bell Sprayer. *Journal of Electrostatics*, Vol. 45(1), 1998.
- [15] Alaa A. Elmoursi. Electrical Characterization of Bell-Type Electrostatic Painting Systems. *IEEE Transactions on Industry Applications*, Vol. 28(5), October 1992.
- [16] Hua Huang and Ming-Chai Lai. Simulation of Spray Transport from Rotary Cup Atomizer using KIVA-3V. In *ICLASS 2000*, Pasadena, California, USA, July 2000.
- [17] J.A. Thorpe. *Elementary Topics in Differential Geometry*. Springer-Verlag., New York, NY, 1979.
- [18] Jeff Petty. personal communication, 2001.

A Revised Asymmetry Term for 2D Deposition Model

The planar deposition model developed in Section 3.1.1 failed to capture the bidirectional asymmetry exhibited in our experiments. The revision to this model presented here is designed to allow the model to capture the more localized asymmetry evident from the bidirectional tests.

For convenience, the basic form of the planar deposition, first given in (1) is repeated here:

$$d(x, y) = K_1 ((1 - K_2) f(x, y) g_1(x, y) + K_2 g_2(x, y)) .$$

The original asymmetry function, given in Section 3.1.1, was defined to be

$$f(x, y) = (1 + K_3 \sin(\text{atan}2(y, x) - \phi)) .$$

We now expand this definition to include the bidirectional asymmetry, and define the new asymmetry function as

$$f(x, y) = \left(1 + K_3 \sin(\beta - \phi) + K_4 \exp - \frac{(\cos(\beta - \rho) - 1)^2}{2\sigma_\rho^2} \right) , \quad (22)$$

where $\beta = \text{atan}2(y, x)$, K_4 weights the new asymmetry term, ρ is the location of the new asymmetry term, and σ_{rho} is the standard deviation of the new asymmetry term. The original normalizing term for the revolved Gaussian, γ , must be redefined. The new γ will be determined by numerical integration such that

$$\gamma = \int \int f(x, y) g_1(x, y) dy dx .$$

Figure 31 represents a potential instance of this new deposition model. As of this writing, the updated model given here has not been experimentally validated.

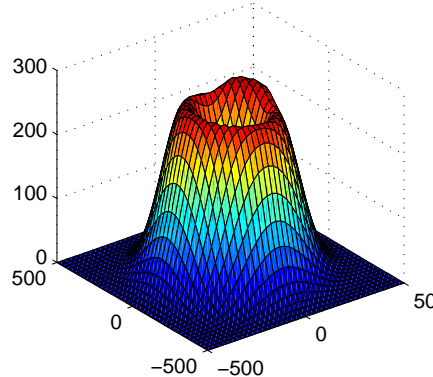


Figure 31: 2D Deposition model with bilateral asymmetry.

B Experimental Data

ABBFlexibleAutomation
ProcessValidationLab
TestingProgram

Ford/CarnegieMellonTests

Paint-Material	Toreador Red (New Batch - June '01)
Date	9/27/2001
Bell	923

Percent-Solids-Vol.	Estimated
Specific-Weight-(lbs/gal)	
Percent-Solids-Weight	
Viscosity-(Ford-44-Cup)	17.89-sec. @80°F

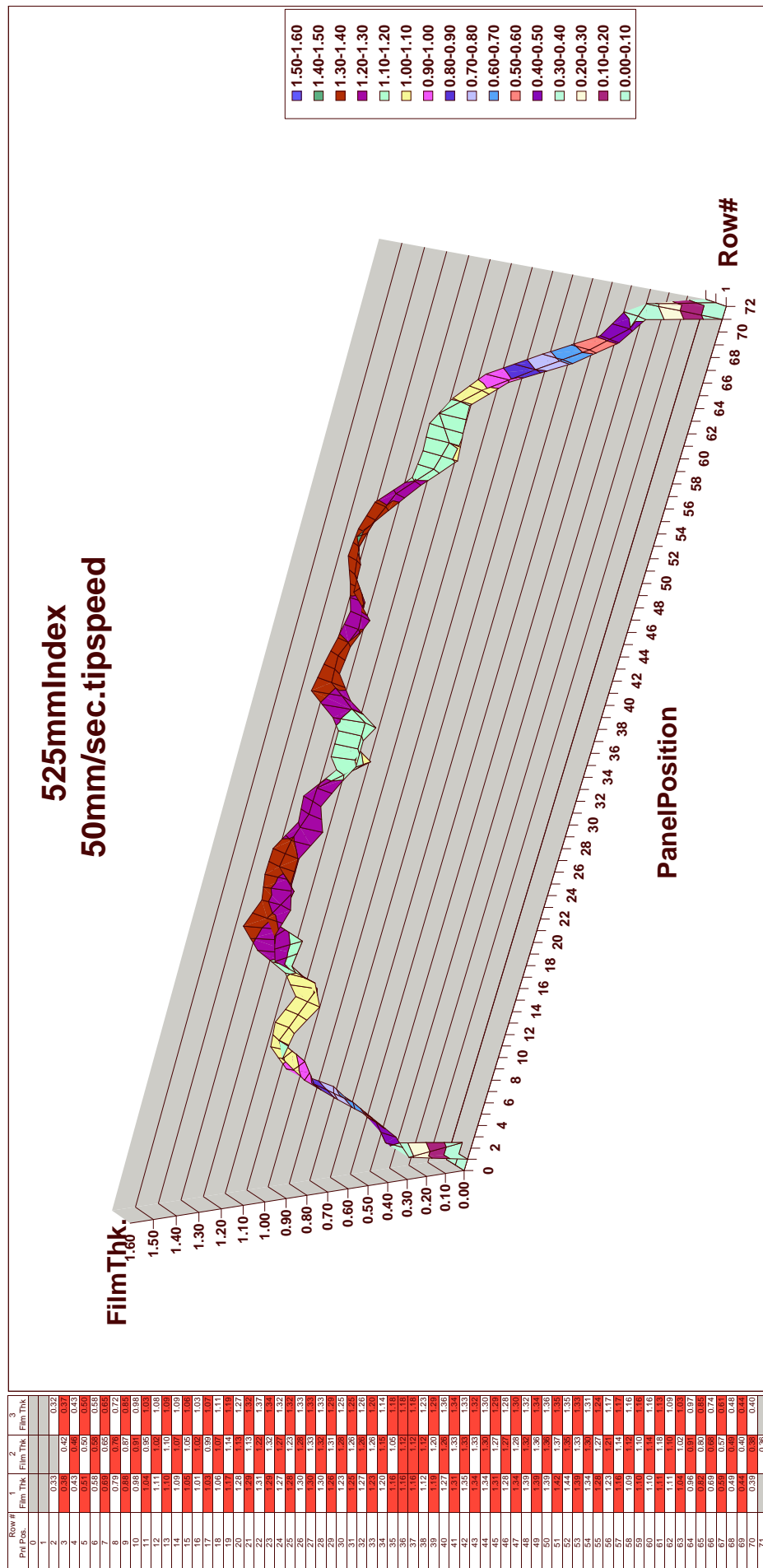
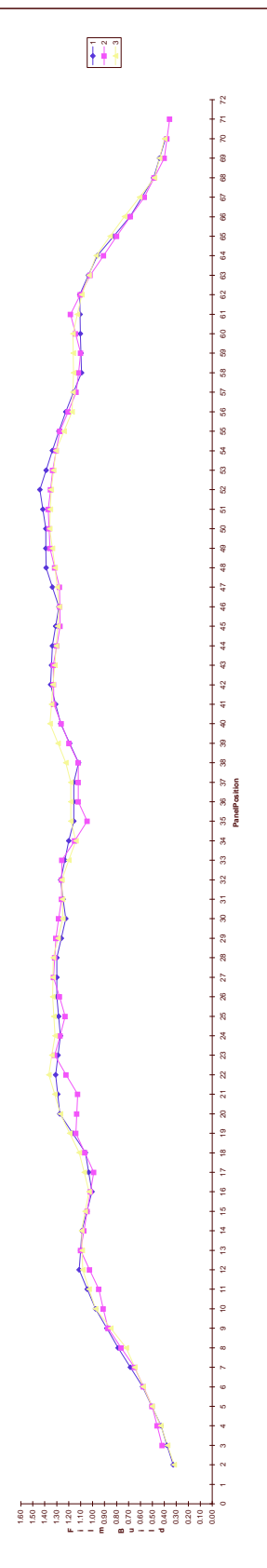
Test-Panel#	Setpt.-Fluid-Flow-cc/min	Shaping-Air-Nl/min	Bell-Speed-KRPM	Bell-Cup-Size	Target-Distance	H.V.-	Notes
9-26-1 & 2	150	250	30	50	10	90	Using 2N1408 50mm Bell Cup and "Annular Slit" S. A. Ring w/200mm repulsion ring. Applicator index 525mm, tip speed 50mm/sec, 3 vertical strokes.
9-26-3 & 4	150	250	30	50	10	90	Using 2N1408 50mm Bell Cup and "Annular Slit" S. A. Ring w/200mm repulsion ring. Applicator index 577mm, tip speed 50mm/sec, 3 vertical strokes.
9-26-5 & 6	150	250	30	50	10	90	Using 2N1408 50mm Bell Cup and "Annular Slit" S. A. Ring w/200mm repulsion ring. Applicator index 525mm, tip speed 50mm/sec, 3 vertical strokes.
9-26-7 & 8	150	250	30	50	10	90	Using 2N1408 50mm Bell Cup and "Annular Slit" S. A. Ring w/200mm repulsion ring. Applicator index 577mm, tip speed 250mm/sec, 3 vertical strokes.

Conveyor Speed (FPM)	Stationary
Gun Trigger On Length (Inches)	Manual Trig.
Booth Air Flow (FPM)	
Booth Temperature (F)	
Booth Humidity (%RH)	

Using 2811408 50mm Bell Cup and "Annular" S.A. Ring w/20mm repulsion ring. Applicator index 52mm, sp speed 50mm/sec, 3 vertical strokes.

Lord / Carnegie Mellon Test

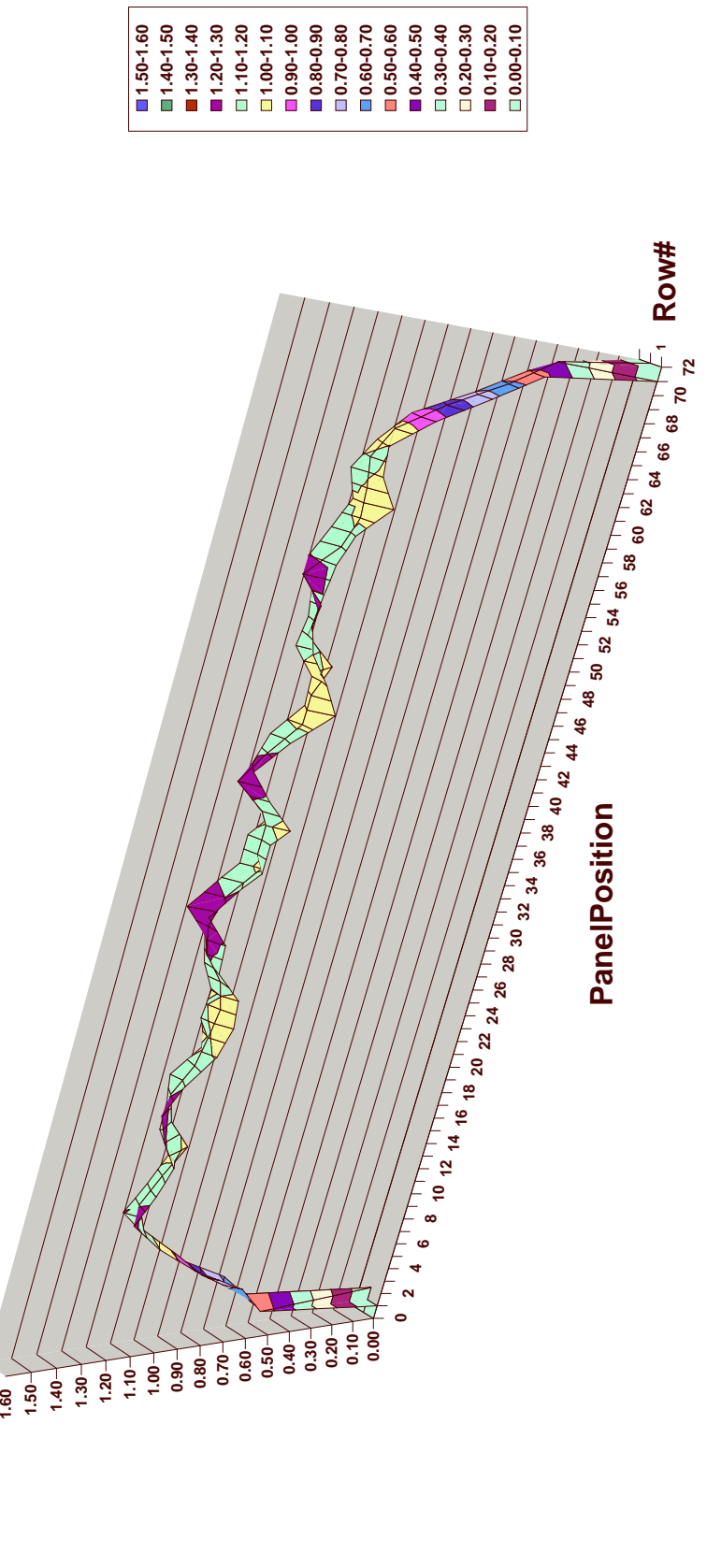
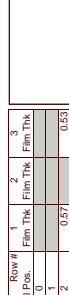
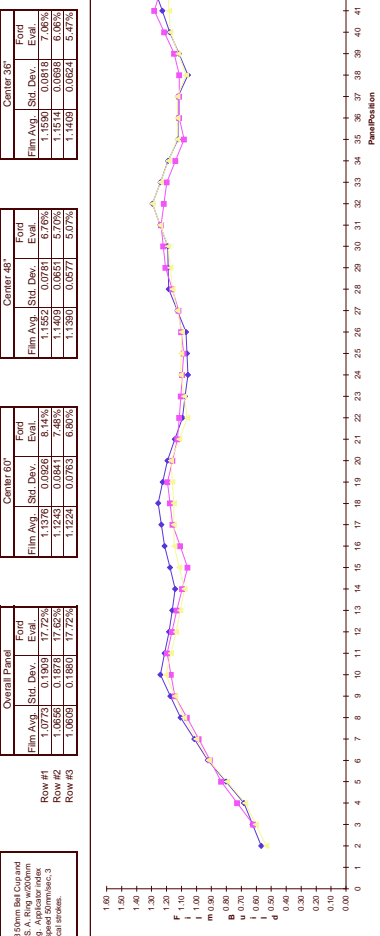
Using 2BN/408/50mm Bel Cup and
"Annular" Siz. A, Ring w/20mm index
repulsion, tip speed 50mm/sec. 3
vertical strokes.



Using 21N140 50mm Bell Cup and
"Annular Sat" S.A. Ring w/200mm
repulsion ring. Applicator index
52.5mm, tip speed 50mm/sec., 3
vertical strokes.

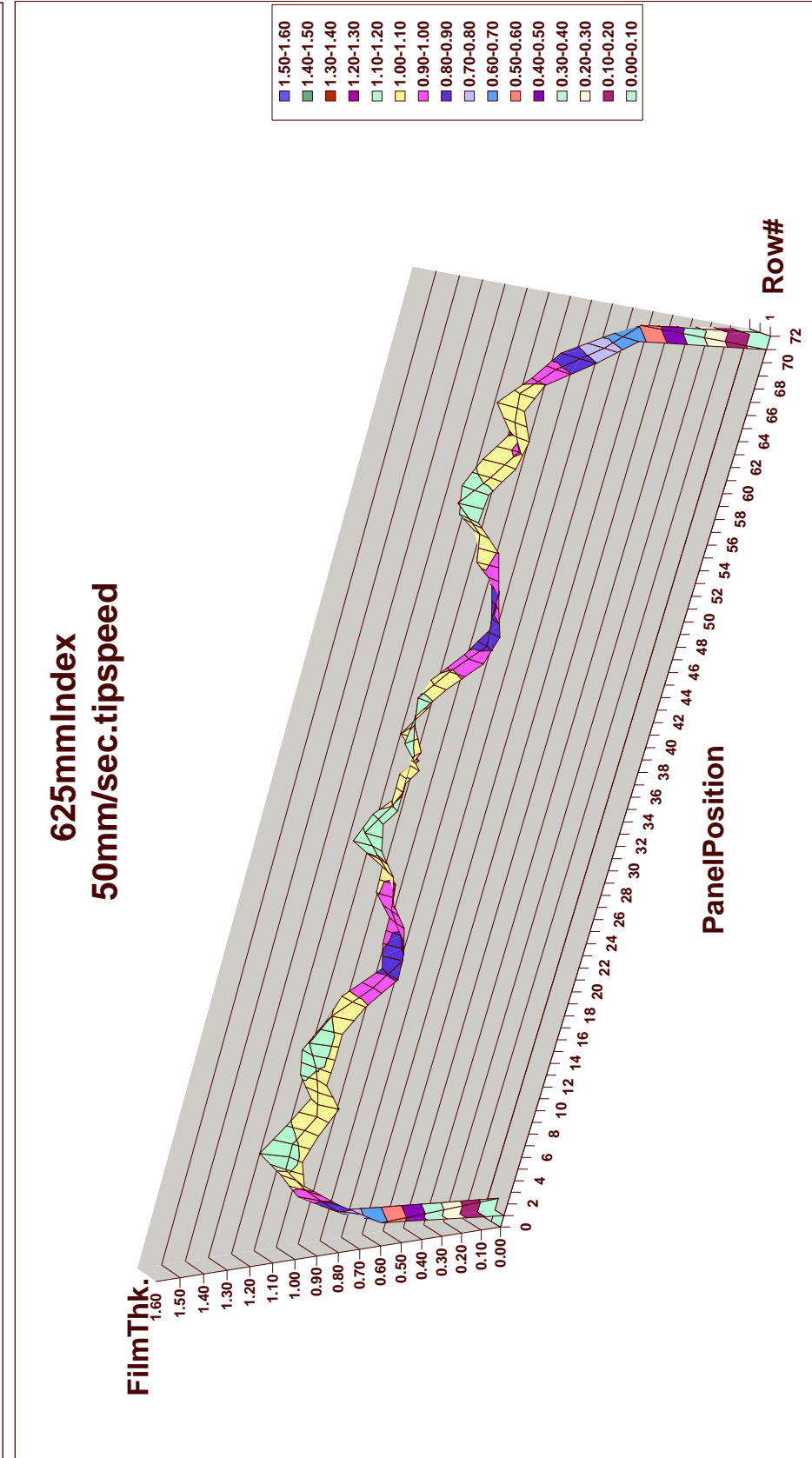
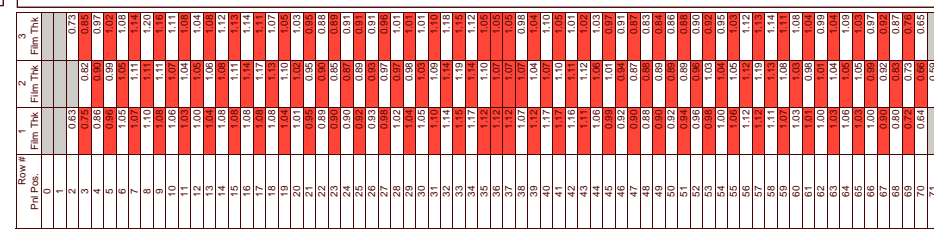
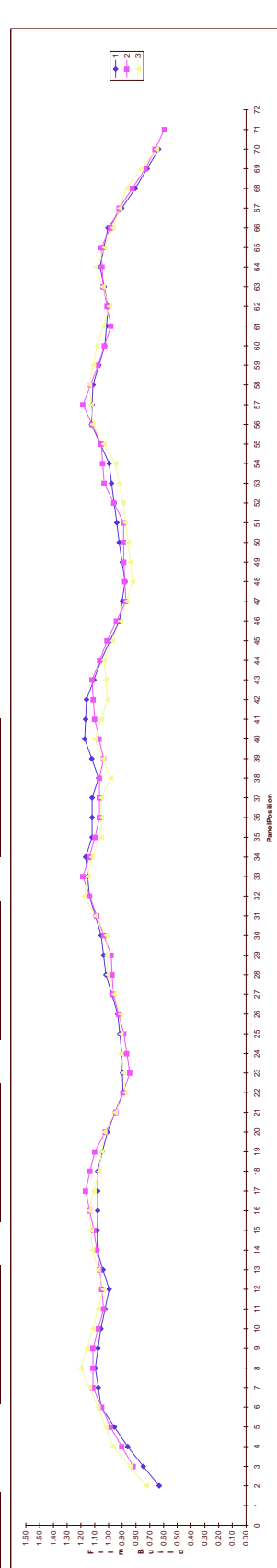
Ford / Carnegie Mellon Test

Date	9/27/2001
Test Number #	2-6-5 & 4
Using 2BN-40/50mm Ball Cup and Pendulum Set. A. Impact width 20mm B. Pendulum length 100mm C. Impact velocity 5m/s D. Impact force 50N E. Impact distance 50mm F. Impact time 100ms G. Impact energy 3 H. Impact strokes: 3	



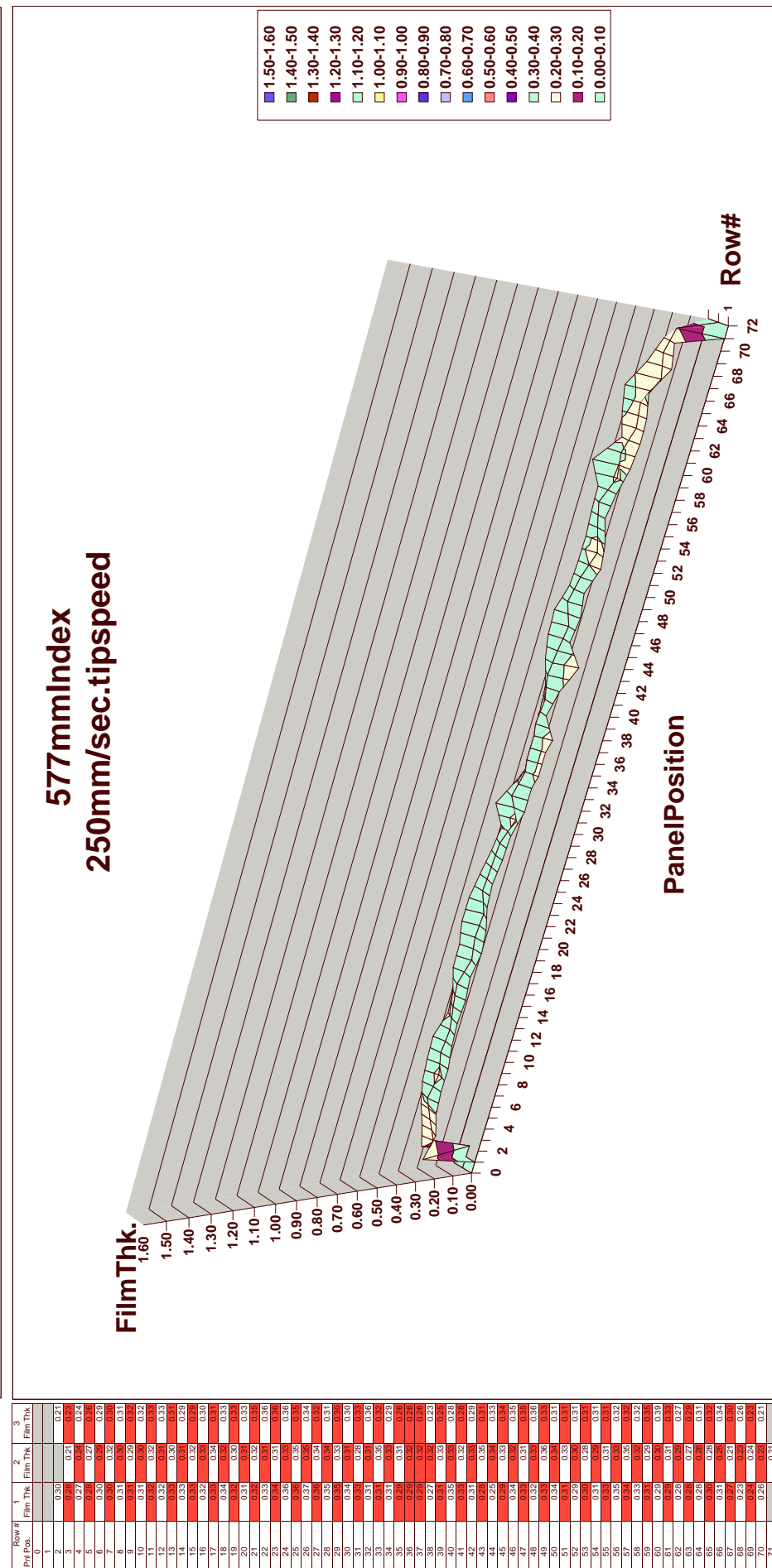
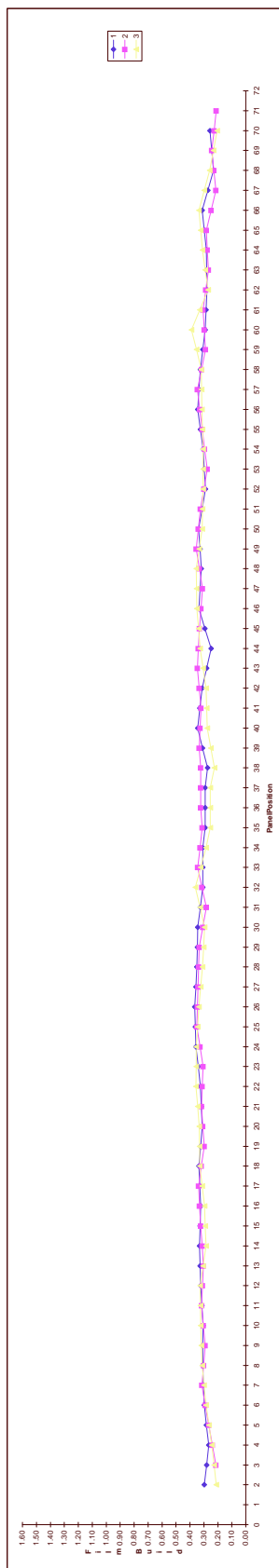
Date	9/27/2001
Test Number #	92705 & 6
Overall Panel	
Film Avg.	0.003
Std Dev.	0.003
Row #1	1.0016
Row #2	1.0016
Row #3	0.9987

Veritas SRI, A, B, C, D, E
replicating wind tunnel
Schlieren, 10 speed Synthesis, 3
Vehicle tested.
Shanein, NHTSA
RPNAk (1000)
30
Bell Club rpm
50
Target Test, in.
10
T.V., KU
80



Using 2 N108 50mm Bell Cup and
"Aerudar Str." S.A. Ring w/200mm
Repulsion ring. Applicator index
52.5mm. sp speed 50mm/sec. 3
vertical strokes.

Ford / Carnegie Mellon Test



**ABBFlexibleAutomation
ProcessValidationLab
TestingProgram**

Ford/CarnegieMellonTests

Paint Material	Toreador Red (New Batch - June '01)
Date	9/28/2001
Bell	923

Test Panel #	Flow ccm/min	Shaping Air Nl/min	Bell Speed KRPm	Bell Cup Size	Target Distance	H.V.	Notes
9-27-1	180	260	40	50	10	80	
9-27-2	150	250	30	50	10	80	Using 2N1408 50mm Bell Cup and "Annular Slit" S. A. Ring w/200mm repulsion ring. KTP program (400-450mm/sec. tip speed), vertical strokes.
9-27-3	150	250	30	50	10	80	Using 2N1408 50mm Bell Cup and "Annular Slit" S. A. Ring w/200mm repulsion ring. KTP program (400-450mm/sec. tip speed), vertical strokes.
9-27-4	150	250	30	50	10	80	Using 2N1408 50mm Bell Cup and "Annular Slit" S. A. Ring w/200mm repulsion ring. CMU modified program (UP100) -100mm/sec. tip speed, vertical strokes.
9-27-5	150	250	30	50	10	80	Using 2N1408 50mm Bell Cup and "Annular Slit" S. A. Ring w/200mm repulsion ring. CMU program, 100mm/sec. tip speed, horizontal aligned strokes.
9-27-6	150	250	30	50	10	80	Using 2N1408 50mm Bell Cup and "Annular Slit" S. A. Ring w/200mm repulsion ring. Single, horizontal, robot stroke at vertical midpoint of panel, at 250mm/sec. tip speed.
9-27-7	150	250	30	50	10	80	Using 2N1408 50mm Bell Cup and "Annular Slit" S. A. Ring w/200mm repulsion ring. Single, horizontal, robot stroke at vertical midpoint of panel, at 100mm/sec. tip speed.

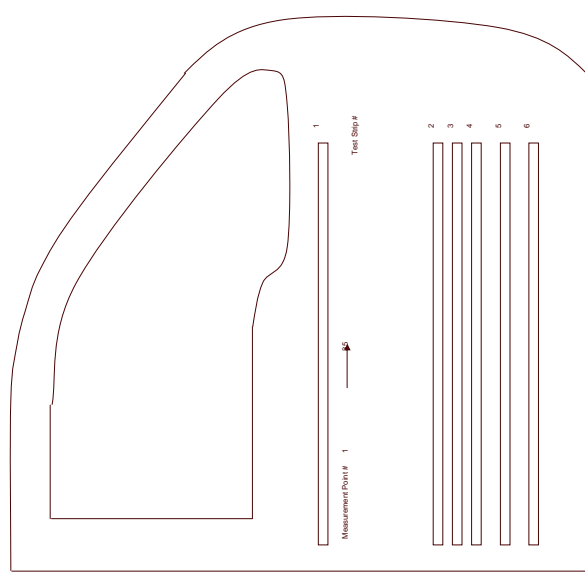
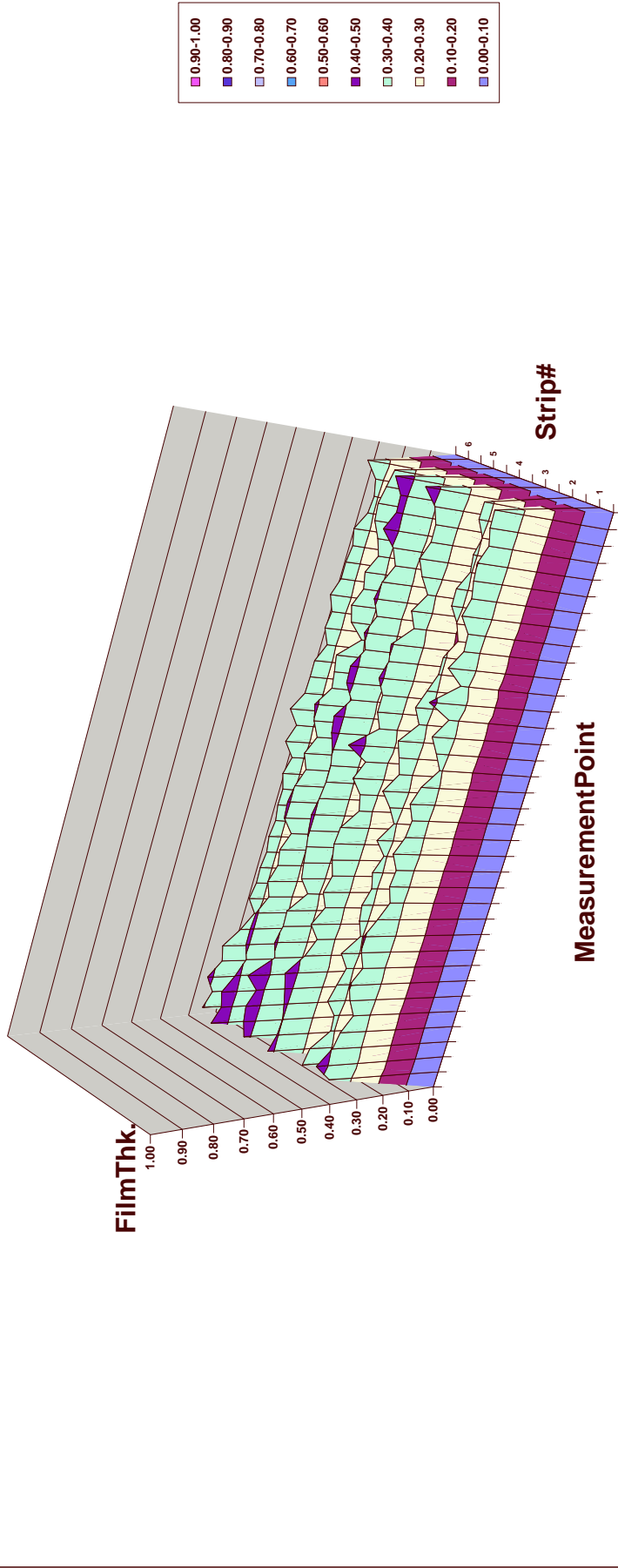
Conveyor Speed (FPM)	N / A
Gun Trigger On Length (Inches)	
Booth Air Flow (FPM)	
Booth Temperature (F)	
Booth Humidity (%RH)	

Percent Solids Vol.	Estimated
Specific Weight (lb/gal)	
Percent Solids Weight	
Viscosity (Ford #4 Cup)	17.89 @80°F

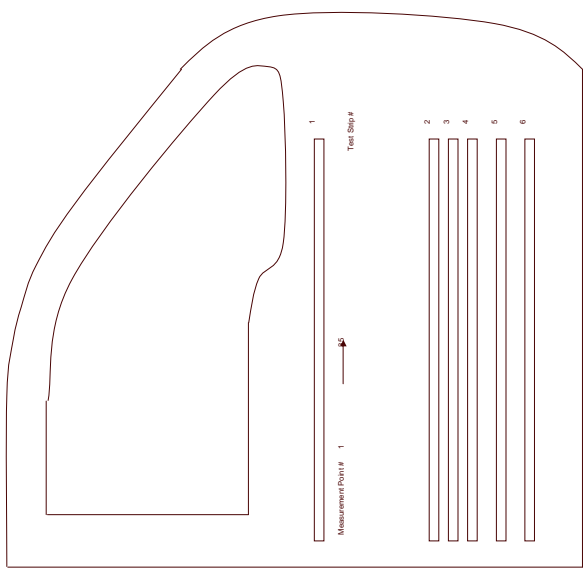
Date	9/26/2009
Test #	9-27-1
Start Time	10:00 AM
Stop Time	1:00 PM
Shaving (N/mm)	260
RFMax (V/mm)	40
Bal. Cap. min.	50
Target Def. in.	10
F.V. Ref.	60

Measurement Point	Film Thk.					
	1	2	3	4	5	6
1	0.37	0.38	0.42	0.42	0.46	0.41
2	0.44	0.39	0.40	0.44	0.44	0.39
3	0.40	0.31	0.40	0.45	0.45	0.42
4	0.39	0.32	0.41	0.43	0.42	0.38
5	0.36	0.36	0.44	0.46	0.44	0.36
6	0.36	0.36	0.44	0.46	0.44	0.36
7	0.41	0.32	0.39	0.41	0.41	0.31
8	0.37	0.36	0.36	0.40	0.41	0.35
9	0.40	0.31	0.40	0.40	0.38	0.34
10	0.31	0.33	0.30	0.30	0.34	0.30
11	0.33	0.33	0.34	0.34	0.34	0.34
12	0.35	0.32	0.37	0.38	0.39	0.34
13	0.36	0.33	0.33	0.39	0.36	0.33
14	0.36	0.31	0.40	0.40	0.40	0.34
15	0.35	0.35	0.32	0.32	0.34	0.32
16	0.36	0.34	0.36	0.36	0.36	0.34
17	0.36	0.39	0.40	0.39	0.38	0.40
18	0.38	0.39	0.40	0.39	0.40	0.38
19	0.36	0.34	0.37	0.40	0.40	0.37
20	0.31	0.36	0.35	0.42	0.40	0.36
21	0.34	0.39	0.39	0.42	0.40	0.36
22	0.36	0.33	0.38	0.39	0.37	0.36
23	0.33	0.36	0.38	0.42	0.38	0.36
24	0.42	0.33	0.42	0.43	0.39	0.33
25	0.33	0.31	0.42	0.42	0.41	0.33
26	0.35	0.35	0.34	0.38	0.38	0.37
27	0.36	0.32	0.37	0.41	0.36	0.35
28	0.40	0.34	0.33	0.40	0.37	0.35
29	0.38	0.36	0.37	0.41	0.36	0.34
30	0.42	0.34	0.31	0.39	0.45	0.34
31	0.38	0.30	0.37	0.42	0.39	0.32
32	0.39	0.33	0.40	0.42	0.39	0.33
33	0.38	0.33	0.40	0.42	0.39	0.31
34	0.39	0.33	0.40	0.42	0.39	0.33
35	0.40	0.33	0.40	0.42	0.39	0.33
36	0.38	0.33	0.40	0.42	0.39	0.33
37	0.38	0.33	0.40	0.42	0.39	0.33
38	0.38	0.33	0.40	0.42	0.39	0.33
39	0.38	0.33	0.40	0.42	0.39	0.33
40	0.38	0.33	0.40	0.42	0.39	0.33

Test#9-27-1

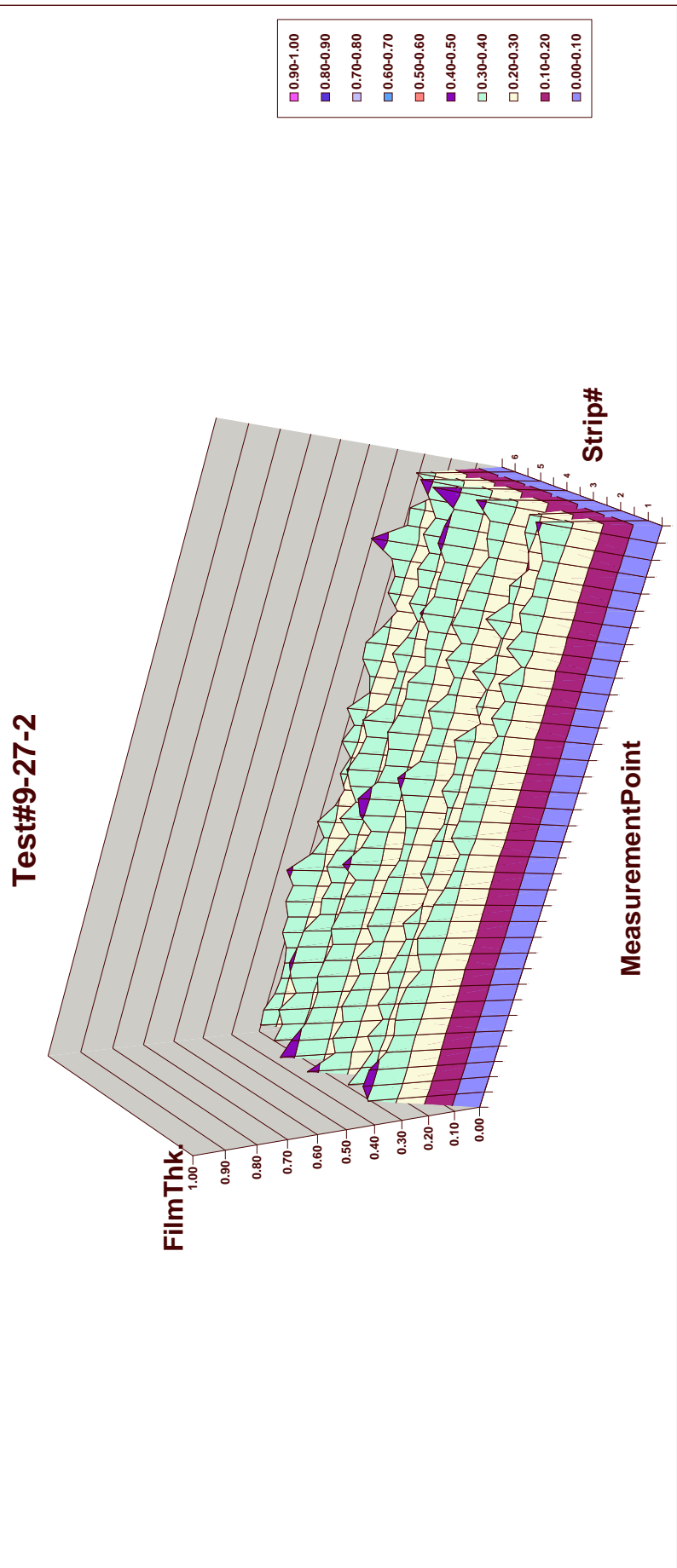


Date	9/26/2009
Test #	9-27-2
Setup:	Uvco200A030 Sprayed Bed Cope w/Arched S. & K Program:000-Bottomline-tp quiescent venting tests.
Setup:	150 Spray (N/mm)
Reflux (L/min)	30
Bed Cap. min.	50
Target Dst. in.	10
P.V. Ref.	60

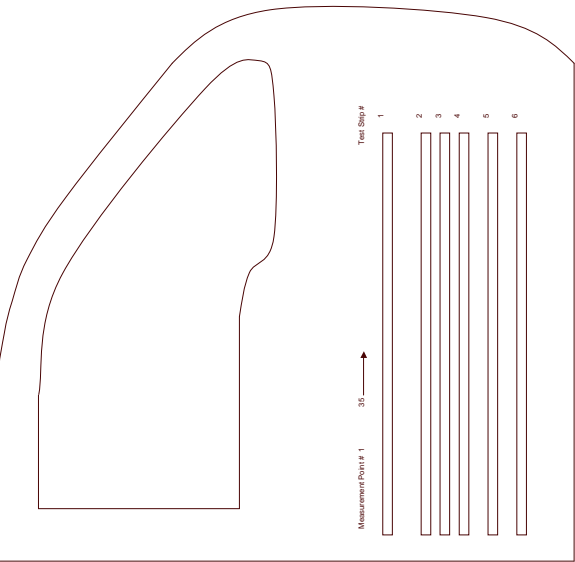


Measurement Point	Overall Strip					
	1	2	3	4	5	6
1	0.40	0.38	0.44	0.45	0.39	0.35
2	0.43	0.36	0.35	0.43	0.37	0.36
3	0.42	0.32	0.38	0.39	0.40	0.32
4	0.38	0.36	0.36	0.39	0.36	0.35
5	0.36	0.35	0.35	0.35	0.35	0.35
6	0.36	0.35	0.35	0.35	0.35	0.35
7	0.39	0.33	0.39	0.40	0.41	0.37
8	0.36	0.38	0.38	0.39	0.37	0.37
9	0.34	0.34	0.33	0.40	0.35	0.39
10	0.36	0.32	0.37	0.37	0.36	0.36
11	0.36	0.32	0.37	0.37	0.36	0.36
12	0.36	0.35	0.36	0.36	0.34	0.34
13	0.35	0.35	0.35	0.36	0.36	0.35
14	0.34	0.35	0.33	0.42	0.36	0.32
15	0.33	0.33	0.33	0.33	0.33	0.33
16	0.36	0.31	0.36	0.44	0.38	0.32
17	0.36	0.32	0.39	0.39	0.41	0.36
18	0.37	0.32	0.39	0.39	0.38	0.35
19	0.37	0.32	0.39	0.42	0.38	0.35
20	0.37	0.33	0.39	0.39	0.38	0.35
21	0.36	0.32	0.39	0.39	0.37	0.32
22	0.36	0.32	0.39	0.35	0.38	0.30
23	0.32	0.38	0.38	0.37	0.33	0.32
24	0.37	0.32	0.33	0.38	0.32	0.36
25	0.34	0.35	0.33	0.33	0.32	0.33
26	0.31	0.31	0.34	0.36	0.31	0.29
27	0.31	0.31	0.39	0.41	0.35	0.34
28	0.35	0.36	0.38	0.38	0.34	0.33
29	0.36	0.32	0.37	0.37	0.36	0.32
30	0.34	0.32	0.37	0.37	0.34	0.34
31	0.36	0.36	0.38	0.38	0.38	0.34
32	0.36	0.36	0.38	0.38	0.38	0.34
33	0.34	0.36	0.36	0.36	0.41	0.35
34	0.38	0.34	0.36	0.40	0.39	0.35
35	0.34	0.34	0.33	0.40	0.44	0.36
36	0.34	0.34	0.33	0.40	0.44	0.36

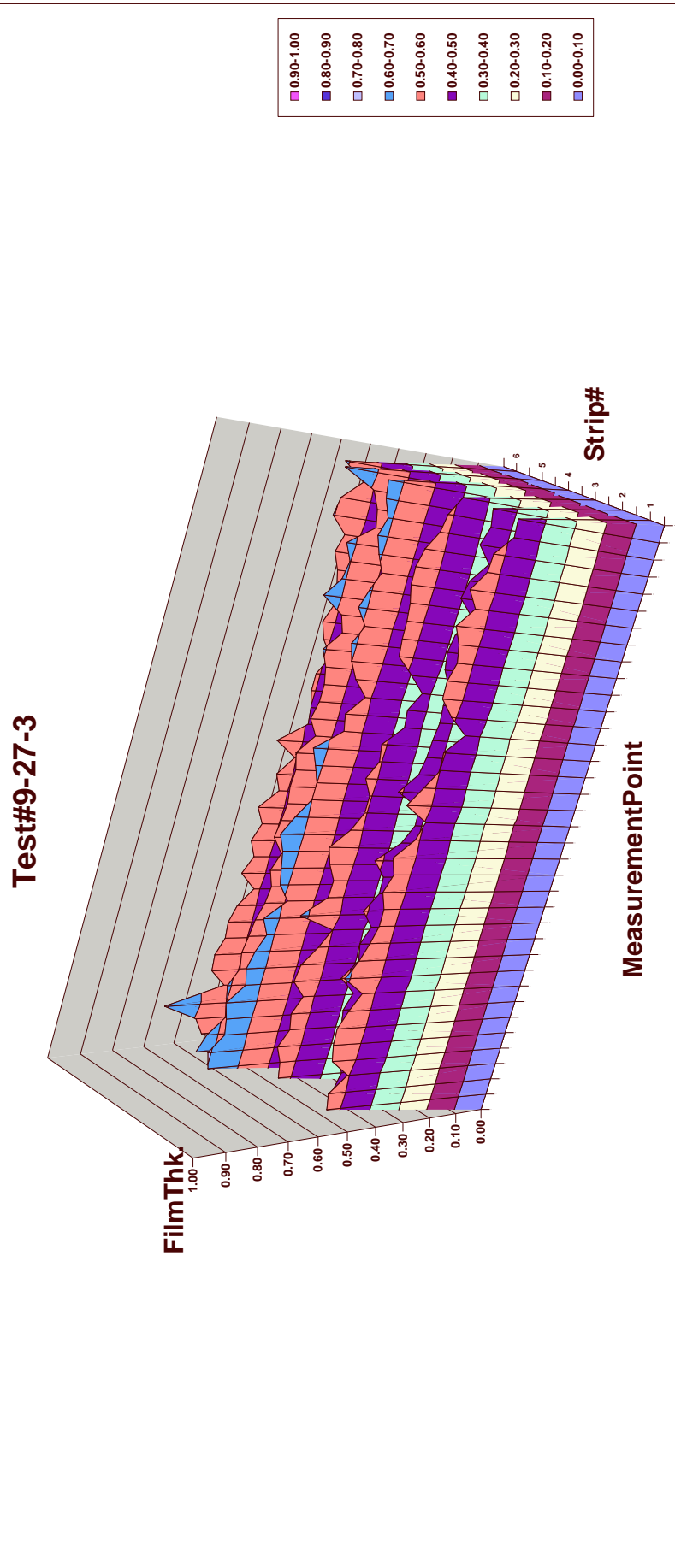
Test#9-27-2



Date	9/26/2009
Test #	9-27-3
Setup:	1500
Shear (N/mm)	260
RFMax (kW)	30
Bal. Cap. min.	50
Target Def. in.	10
F.V. Ref.	60

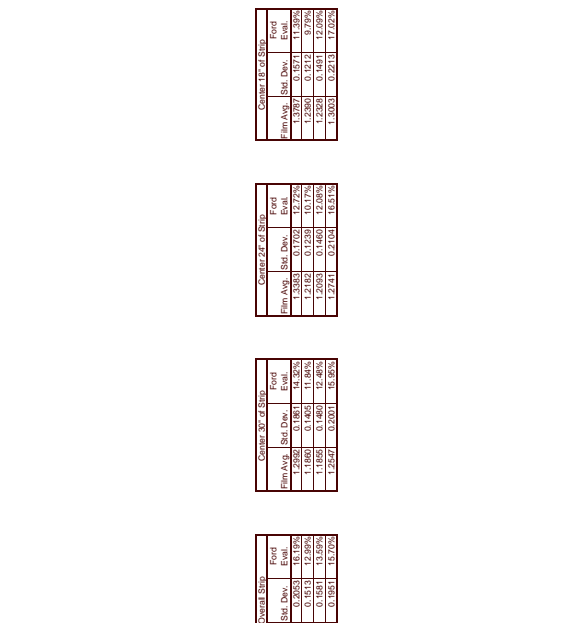
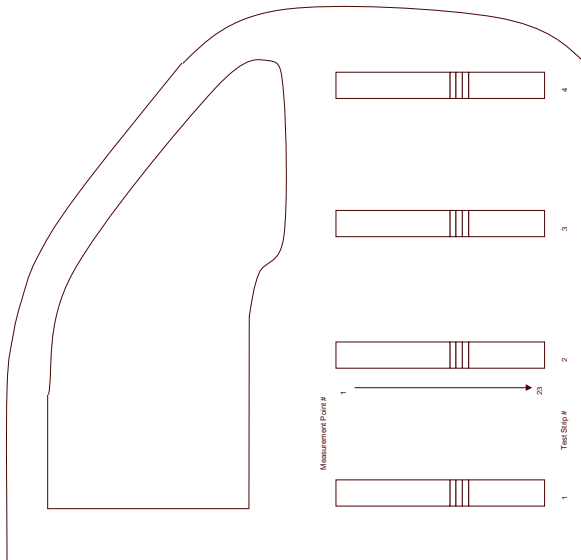


Test#9-27-3

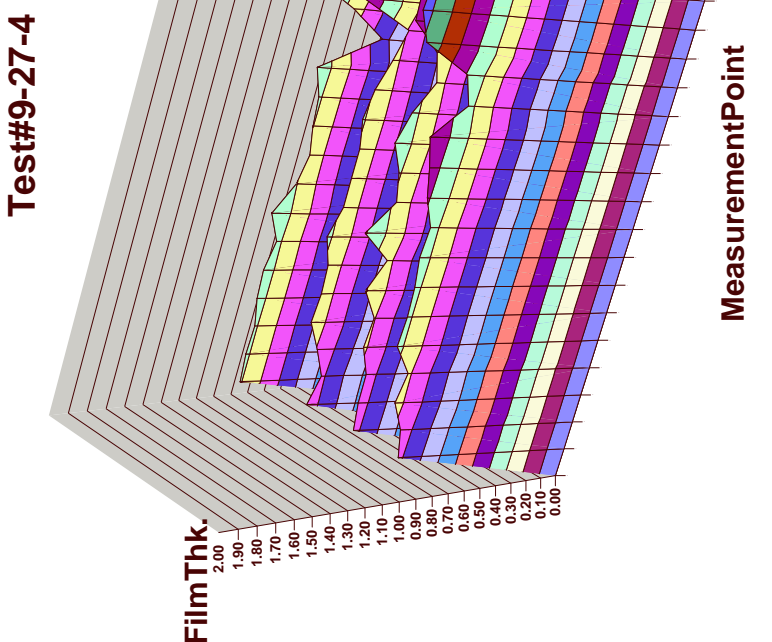


Date	9/26/2010
Test #	9-27-4
Overall Film Type	Spun-Bleat Copolymer
Overall Film Thickness	0.250
Overall Film Width	150
Shaving (N/mm)	260
ReMark X (mm)	30
Bal. Cuts (mm)	50
Total Def. (in.)	10
F.V. (in.)	60

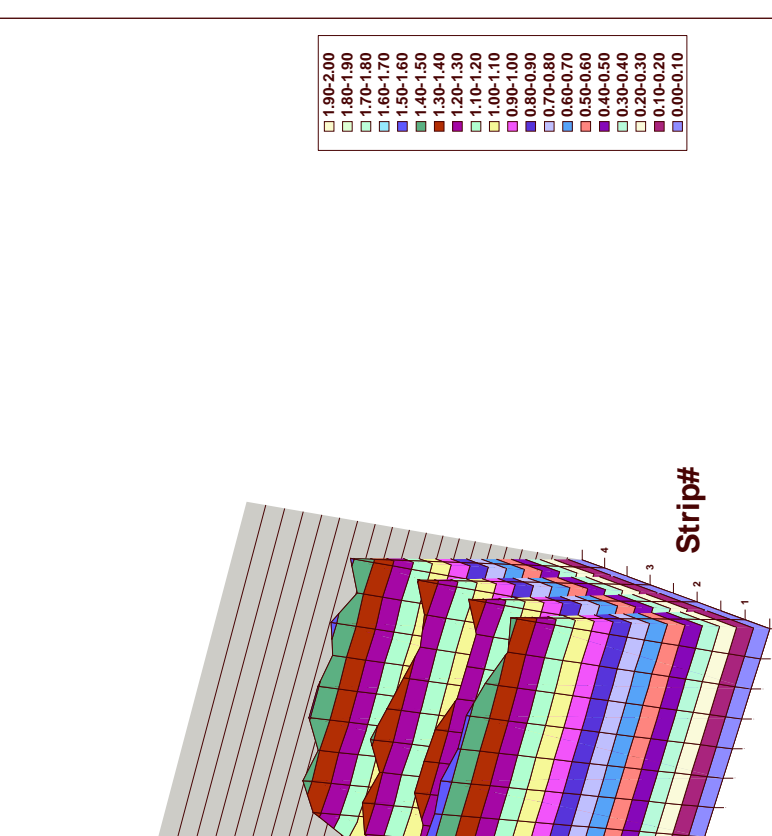
Measurement Point	1	2	3	4
Panel Layout				
1	1.13	1.03	1.13	1.20
2	1.16	1.21	1.08	1.10
3	1.14	1.06	1.08	1.07
4	1.13	1.22	1.11	1.09
5	1.13	1.22	1.11	1.10
6	1.13	1.20	1.14	1.12
7	1.13	1.13	1.13	1.13
8	1.13	1.13	1.13	1.13
9	1.14	1.06	1.08	1.07
10	1.13	1.22	1.11	1.09
11	1.13	1.22	1.11	1.10
12	1.16	1.14	1.08	1.12
13	1.13	1.04	1.03	0.95
14	1.13	1.03	0.99	1.06
15	1.48	1.27	1.30	1.34
16	1.35	1.29	1.35	1.45
17	1.54	1.32	1.32	1.45
18	1.56	1.38	1.42	1.51
19	1.51	1.39	1.37	1.51
20	1.52	1.26	1.33	1.47
21	1.37	1.29	1.29	1.33
22	1.33	1.29	1.29	1.33
23	1.43	1.30	1.41	1.52
24	1.43	1.30	1.41	1.52



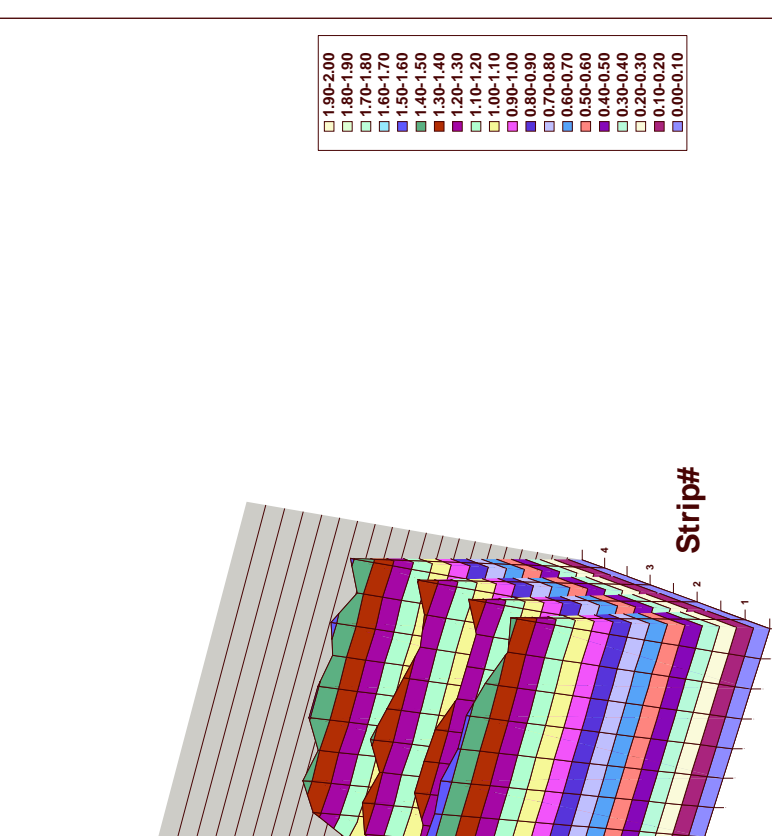
FilmThk.



FilmThk.



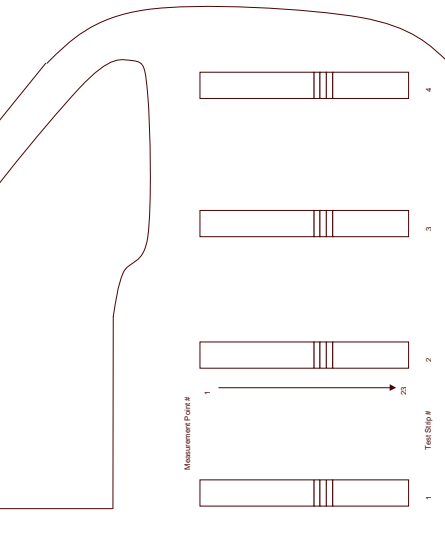
FilmThk.



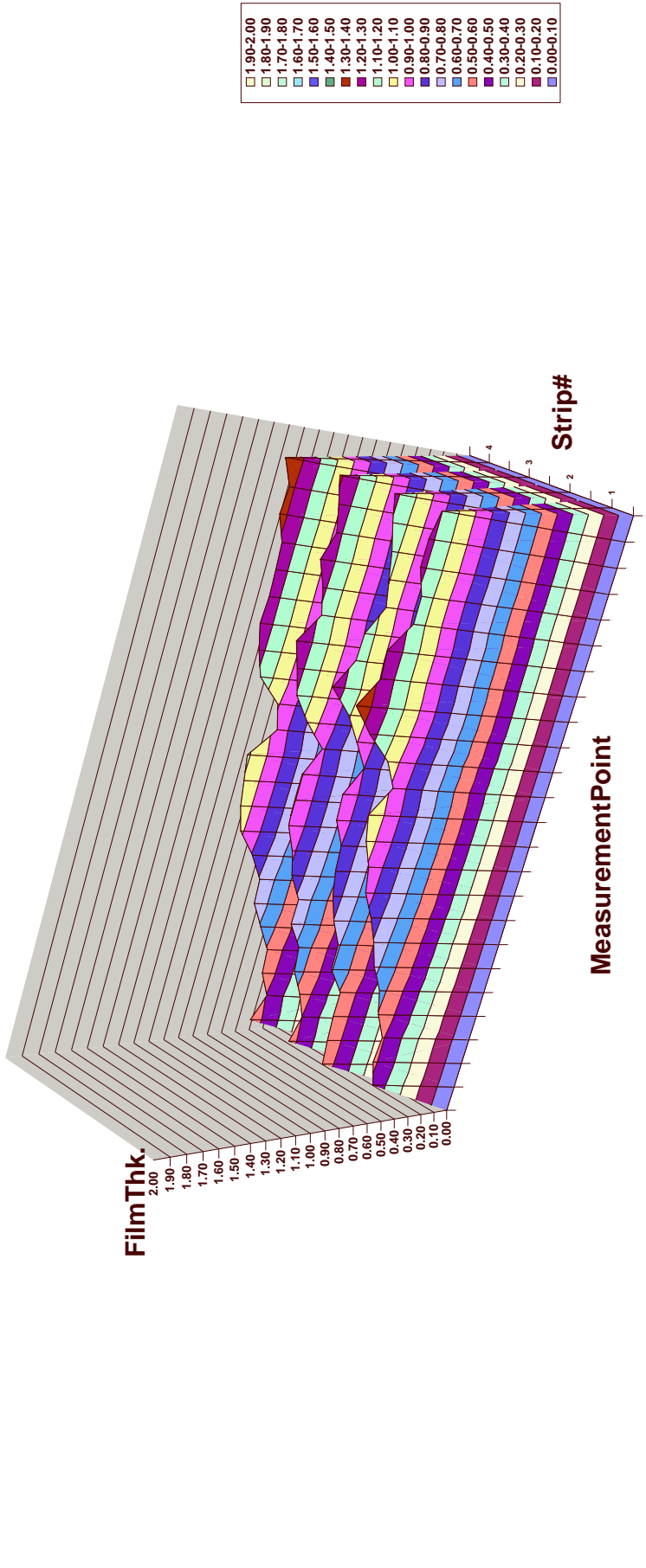
FilmThk.

Date	9/26/2009
Test #	9-27-5
Sheet	150
Shaving (N/mm)	260
RFMax (V/mm)	30
Bal. Cap. min.	50
Total Def. in.	10
P.V. Ref.	60

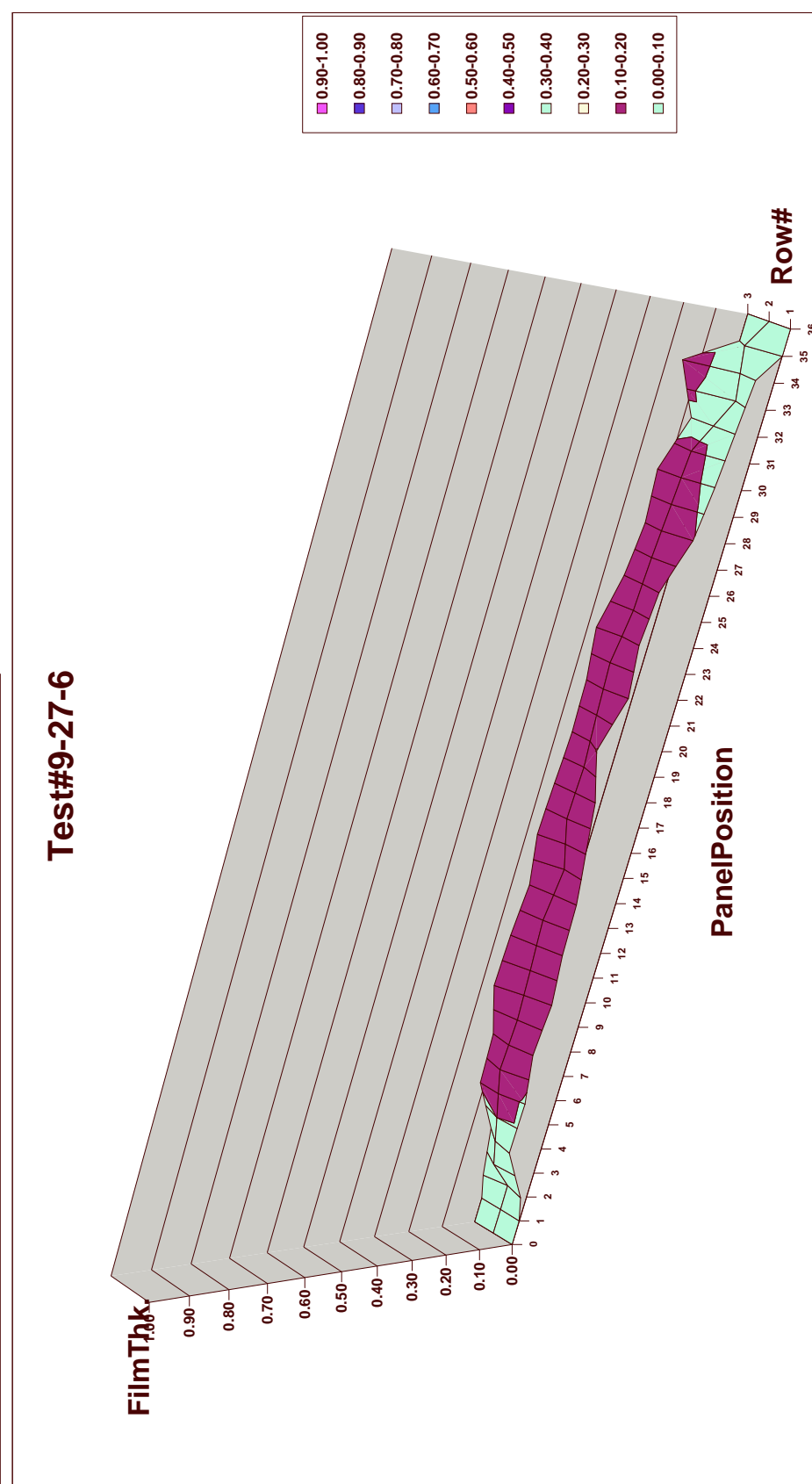
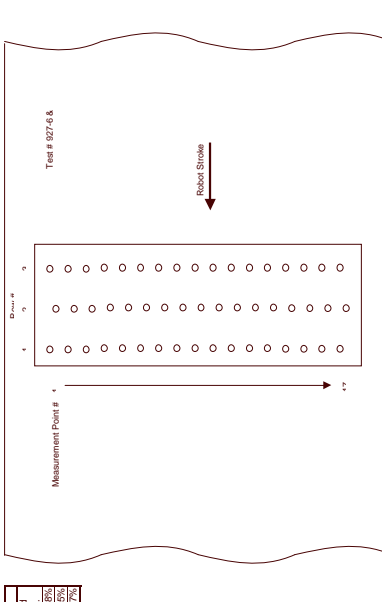
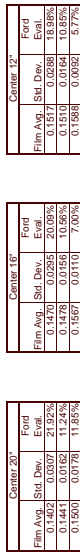
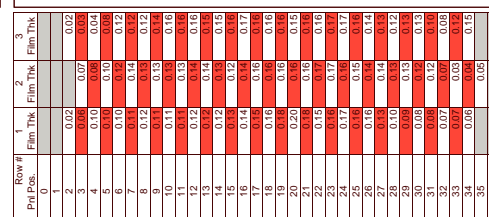
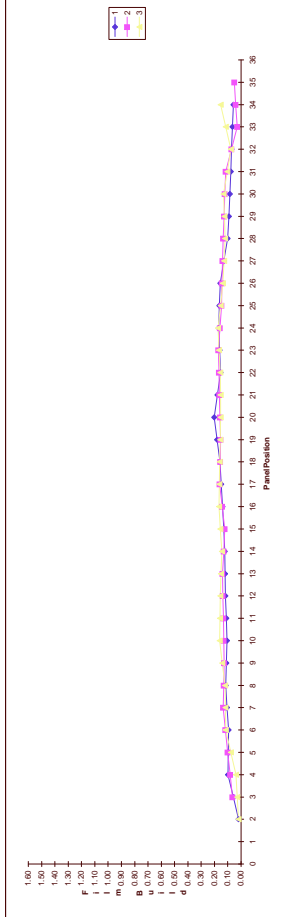
Measurement Point	1	2	3	4
Film Thk.	0.47	0.52	0.54	0.56
1	0.52	0.58	0.50	0.49
2	0.51	0.59	0.57	0.58
3	0.55	0.59	0.65	0.59
4	0.55	0.71	0.67	0.63
5	0.75	0.78	0.79	0.79
6	0.79	0.80	0.78	0.79
7	0.96	0.95	0.97	0.98
8	0.95	0.99	0.92	1.02
9	1.09	1.04	1.00	1.07
10	1.16	1.08	1.09	1.12
11	1.16	0.98	1.00	1.12
12	1.17	1.17	1.17	1.22
13	1.17	1.14	1.14	1.27
14	1.07	1.00	1.07	1.01
15	1.25	1.11	1.19	1.18
16	1.35	1.27	1.24	1.24
17	1.29	1.17	1.23	1.23
18	1.26	1.16	1.18	1.22
19	1.17	1.07	1.22	1.28
20	1.17	1.14	1.20	1.28
21	1.25	1.14	1.22	1.24
22	1.20	1.19	1.23	1.24
23	1.26	1.20	1.32	1.41
24				



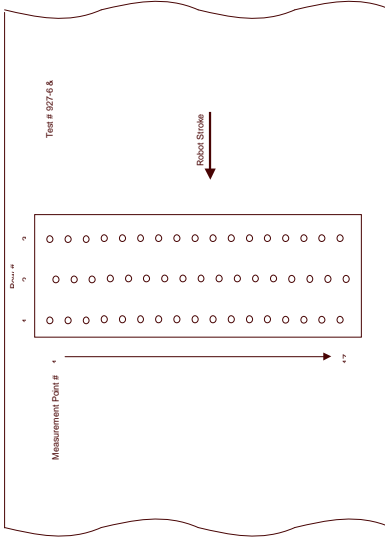
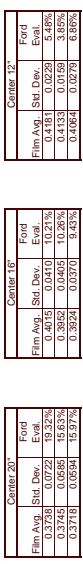
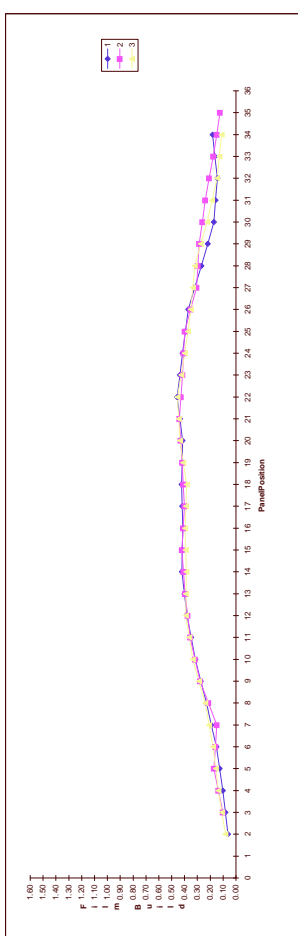
Test#9-27-5



Using 2N1408 50mm Bel Cup and "Amidar Slt" S. A. Ring w/200mm repulsion ring. Single, horizontal, robot stroke at vertical midpoint of plane, at 250mm/sec. tip speed.



Using 2N1408 50mm Ball Cup and
"Annular Star" S. A. Ring w/200nm
repulsion ring. Single, horizontal,
robot strike at vertical midpoint of
panel, at 100mm/sec. tip speed.



Test#9-27-7

